Thermal conductivity of materials under pressure

Yan Zhou[1], *Zuo-Yuan Dong*[1], *Wen-Pin Hsieh*[2], *Alexander F. Goncharov*[3] *and Xiao-Jia Chen*[1,4] ✉

Abstract | The thermal conductivities of materials are extremely important for many practical applications, such as in understanding the thermal balance and history of the Earth, energy conversion of devices and thermal management of electronics. However, measurements of the thermal conductivity of materials under pressure and understanding of associated thermal transport mechanisms remain some of the most difficult challenges and complex topics in high-pressure research. Breakthroughs in high-pressure experimental techniques enable in situ measurements of thermal conductivity at extreme pressure–temperature conditions. This new capability provides not only a unique insight to understand thermal transport mechanisms in materials but also opportunities to realize reversible modulation of materials' thermal properties. In this Review, we discuss recent progresses in characterization techniques developed at high pressures, in the determination of the thermal conductivity of gases, liquids and solids, as well as in establishing the correlated thermal transport mechanisms. In addition, we focus on the applications of high-pressure and high-temperature experimental simulations of materials in the Earth's interior.

Pressure (P) has long been recognized as an important thermodynamic variable that can adjust or even reversibly modulate many physical properties of materials, including the thermal conductivity that is critical in the understanding of thermal transport in Earth and planetary interiors and in condensed matter. However, research was limited to relatively low pressures for a long time, owing to previous unattainability in apparatus and techniques, until the turn of this century, when the megabar (100 GPa) pressure diamond anvil cell (DAC), together with a series of in-laboratory integrated characterization techniques, were developed[1–5]. Static high-pressure generation techniques primarily consist of piston–cylinder cells (with a pressure limit <10 GPa), multi-anvil cells (with a maximum pressure of ~90 GPa) and DACs (with a highest pressure up to ~1,000 GPa)[6–12].

The DAC has become the broadest platform for theoretical and experimental research at high pressure. There are several advantages of DACs. Pressure can be conveniently determined and monitored by the fluorescence peak shift of a ruby sphere crystal (widely available until ~100 GPa) placed close to the sample of interest, with an uncertainty of 2–4%, or determined by the diamond Raman peak positions collected from the near-sample diamond anvil (can be calibrated up to ~410 GPa with an uncertainty of ~15%)[13,14]. In addition, DACs have been successfully combined with various physical and chemical characterization techniques, in which a hydrostatic, stable and homogeneous or even uniaxial or other deviatoric compressive strain (at least 30%) can be generated without any additional damage to samples[15–22].

Although practical applications and technologies requiring pressures to be as high as GPa levels are quite rare, pressure is a powerful way to study the fundamental properties of materials. It can be used to continuously tune material properties and to test the validity of theoretical predictions at various compression states or other extreme conditions. By exploring the pressure dimension, many unexpected physical properties can emerge, as all material properties are expected to undergo changes at various compression states, demonstrating a crossover from the ordinary condensed-matter regime to a dense-matter physics regime[15,19,21,23–33]. It is not surprising to see electronic, elastic, structural, magnetic and chemical properties being altered drastically upon compression, mainly due to the interatomic bonding and orbital coupling, interlayer wavefunction overlap and valence band splitting being modified[19,21,22,27,31,34,35]. The phononic or vibrational properties can also be greatly changed in many materials at high pressures, and some of them can be directly investigated by in situ Raman spectroscopy and Brillouin scattering techniques[36–39]. More importantly, material properties

[1]*Center for High Pressure Science & Technology Advanced Research, Shanghai, China.*

[2]*Institute of Earth Sciences, Academia Sinica, Taipei, Taiwan.*

[3]*Earth and Planets Laboratory, Carnegie Institution for Science, Washington, DC, USA.*

[4]*School of Science, Harbin Institute of Technology, Shenzhen, China.*

✉*e-mail: xjchen2@gmail.com*

https://doi.org/10.1038/s42254-022-00423-9

Key points

- Thermal characterization techniques have been developed in apparatus such as piston–cylinder cells, multi-anvil cells and diamond anvil cells, for both bulk and thin-film materials, and for both temperature-dependent and pressure-dependent measurements.
- Such high-pressure thermal characterization techniques have been applied to gases, liquids and solids, including thermoelectric materials, Earth materials and semiconductor materials.
- The results of the high-pressure thermal conductivities of various materials are summarized, and the underlying thermal transport mechanisms are discussed.
- Practical applications are given on high-pressure and high-temperature experimental simulations of materials in the Earth's interior.

can be tuned by pressure across the various regimes according to conventional classification, such as insulators, semiconductors and superconductors[15,20,23,26,33,40,41], amorphous and crystalline solids and so on, and unique materials or phases can also be created[42–45].

To investigate these physical and chemical properties under pressure, continued progress has been made in high-pressure characterization techniques applied to samples within the DAC apparatus, including structural, optical, electrical, magnetic and thermal properties[19,21,31,46–48]. For example, the changes of lattice parameters and phase structure and the resultant strain induced by pressure can be accurately obtained by the combination of synchrotron X-ray diffraction with DAC techniques; these developments have resulted in progress, including breakthroughs in exploration of metallic hydrogen and high-temperature superconductors[19,28,29,31]. In addition, some critical phenomena, such as phase evolution, stress state and magnitude, phonon modes and electronic bandgaps, which change upon compression or the equivalent strain, can be sensitively and accurately detected experimentally by combining techniques such as in situ micro-Raman, micro-photoluminescence and absorption spectroscopies with the DAC techniques[15,20–22,24,30,49–52].

Despite such achievements in high-pressure characterization of material properties, thermophysical properties remain one of the most difficult to be reliably and accurately measured at high pressures. Thermophysical properties play crucial roles in thermal transport and thermal management; the latter has been a critical bottleneck in many high-power devices and heat exchange systems, for example, transistors and thermoelectric (TE) devices, and electronic systems in mobile phones and computers[53–56]. The thermophysical properties discussed in this Review are emphasized in non-metallic materials in which phonons are the major heat carriers; these properties mainly involve thermal diffusivity, thermal conductivity (κ), heat capacity, phonon velocity, phonon mean free path (MFP), phonon lifetime, interfacial thermal conductance (ITC) and thermal resistance.

Phonons have a large variation in their frequencies and MFPs; for bulk materials at room temperature, the MFP is normally in the range 1–100 nm, which is within the microstructure scale of bulk materials[57]. However, in micrometre-scale and even nanometre-scale samples, the phonon MFP is comparable or even limited to the sample length or width or thickness, resulting in stronger boundary scatterings and, thus, lowering the κ. In terms of common measurements and applications, κ is the most discussed correlative thermal parameter and can be affected by sample thickness, width and length[58], and by strong point defects or dislocation scatterings and isotope scatterings[59]. κ is a temperature-dependent property and, in different temperature regimes, it varies through different phonon scattering mechanisms; thus, temperature, the most often used external stimulus because of its ready availability, is a useful variable to tune, modulate and control the thermal performance of materials and devices. In addition, strain or pressure can also be used to tune the κ of materials, although this research is still in its early stages due to the challenges in high-pressure thermal characterization techniques[17,18,35,47,48,60–66].

The κ values of some solids and liquids at pressures of only up to a few GPa, determined with errors of a few percent, were summarized in 1984; this summary includes the proposed pressure-dependent thermal transport mechanisms for alkali halides, simple metals and non-metallic liquids being theoretically described[67]. In 2007, the pressure dependences of the thermal properties of some geophysically relevant minerals up to 10 GPa were summarized, reporting the re-examined experimental values of the thermophysical parameters with higher accuracy determined using a contact-free laser flash method[68]. More recently, some theoretical and experimental studies have investigated the effects of pressure on κ in a variety of materials, demonstrating rich high-pressure phenomena[17,18,35,47,48,63–66,69,70]. For example, the κ of solid iron (the primary material in the Earth's core) at core conditions up to 130 GPa and 3,000 K was measured using the pulsed-laser transient heating (TH) method[47]. Knowledge of thermal-physical properties under pressure can also advance understanding of heat transport mechanisms and provide useful guidelines for the tunability of thermal properties via pressure or strain method in thermal management, such as the recent κ measurements of MoS_2 under pressure[35].

This Review focuses on pressure-induced modifications in the thermal conductivities of a range of materials, thermal transport behaviours and mechanisms in different material systems, and thermal applications under pressure ranging from ambient pressure up to megabar pressure. We focus on two major classes of materials: deep Earth's mineral and alloys and TE materials, which greatly benefit from high-pressure investigations. Indeed, understanding the thermal conductivity of the Earth's materials is a key for understanding the deep Earth dynamics and the thermal history of the planet. Conversely, application of pressure on TE materials has been proved to be unique in improving the performances of these materials in devices and elucidating the physical mechanisms of these performances, where thermal conductivity plays an important role.

Fundamentals of thermal transport

In principle, thermal transport has three major components: conduction, radiation and convection. These components have different thermal transport mechanisms and are relevant for the thermal properties of materials in different conditions. Near room temperature, the

effects of radiation are usually very small compared with those of conduction; thus, radiation is often neglected. In this Review, we focus on the thermal conduction of materials.

Heat flux generated and transported by conduction through a material is normally described by Fourier's law of heat conduction (FIG. 1a):

$$\dot{Q} = -\kappa \nabla T \tag{1}$$

where $\dot{Q}$ is the local heat flux (with unit Wm^{-2}), κ is the thermal conductivity of material (with unit $Wm^{-1}K^{-1}$) and ∇T is the temperature gradient through the material thickness (with unit Km^{-1}). K is a macroscopic-scale parameter and is correlated to atomic-level properties mainly through energy carriers such as phonons, electrons and holes. In non-metallic crystals such as semiconductors and some thermoelectrics, the main heat carriers are phonons. The total thermal conductivity (κ) of a crystal involves contributions from a lattice (phonon, κ_l) and an electronic (electron, κ_e) component[71], which is described by

$$\kappa = \kappa_l + \kappa_e = \sum_j \frac{1}{3} C_v v_j l_j + L\sigma_e T \tag{2}$$

where C_v is the molar heat capacity at constant volume; v_j is the phonon group velocity of the jth phonon mode; l_j is the MFP of the jth phonon mode, which can be further expressed as $l_j = v_j \tau_{p,j}$, where $\tau_{p,j}$ is the effective phonon scattering time of the jth phonon mode, including contributions from all scattering factors, such as crystalline boundaries, lattice defects and impurities, electrons, other phonons and van der Waals forces[71–80] (Supplementary Information); L is the Lorenz number; σ_e is the electrical conductivity; and T is the temperature of electrons. In metals, κ is dominated by κ_e owing to the large concentration of free electrons, and

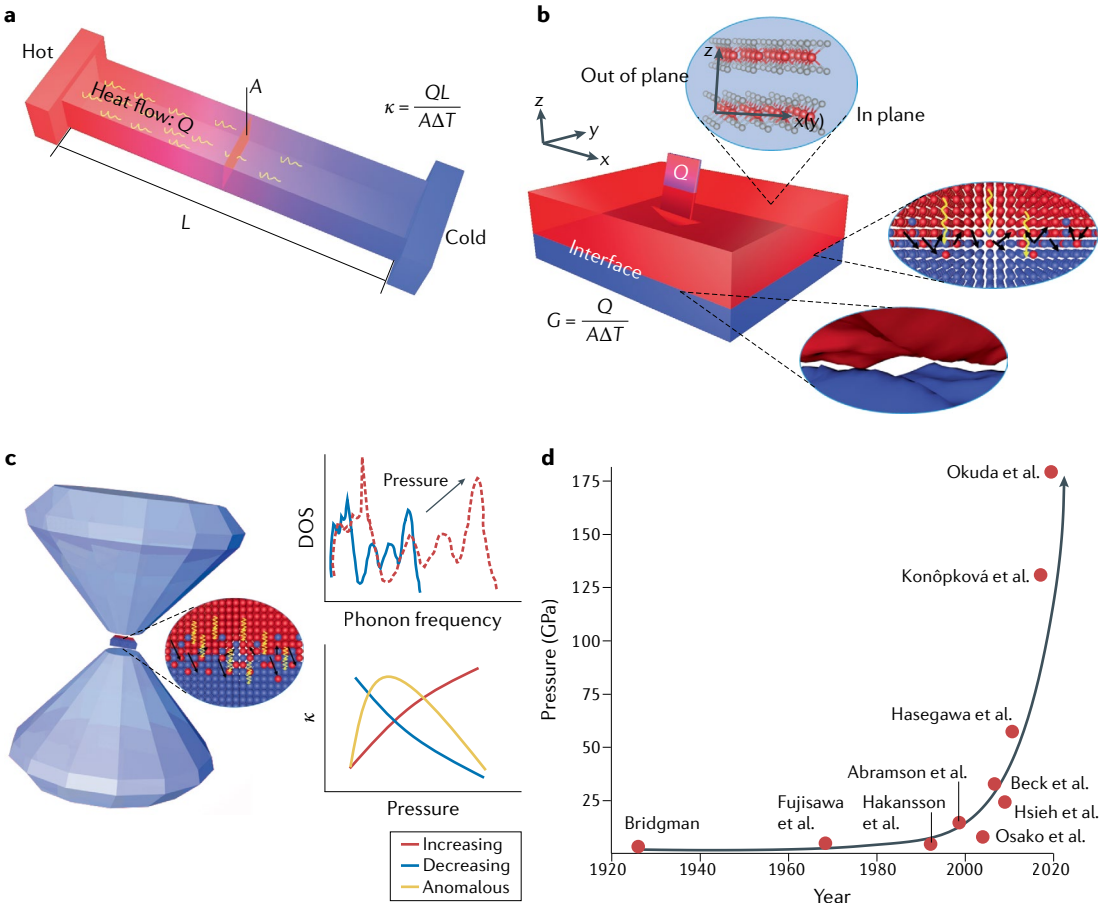

Fig. 1 | **Thermal transport in materials at ambient and high pressures. a** | Parameters in Fourier's law of heat conduction. **b** | Interfacial thermal conductance between two materials and the in-plane and out-of-plane thermal conductivity. Heterointerface contact normally includes conditions of full contact and limited contact, where some air voids are inevitably introduced during the integration (insets); both normally result in a temperature drop ΔT across the interface due to the mismatch of phonon scattering between the two different materials. **c** | Thermal transport at high pressures generated within a diamond anvil cell (left) and the schematic evolution of phonon density of states (DOS) and thermal conductivity with respect to pressure (right). In general, the application of pressure compresses the crystal lattice and extends the phonon frequency range, thereby, promoting the heat-carrying ability of electrons and some phonons, bringing about the modification of thermal conductivity under pressure (increasing trend, decreasing trend and anomalous trend). **d** | Progress in thermal conductivity measurements at high pressures. Data points are representative works; the values of pressure and year are taken from REFS[17,18,47,132,133,148,163,173,177,266]. ΔT, temperature difference from the hot to the cold terminals; A, cross-sectional area; L, length of thermal transport; Q, total thermal energy of heat flow through the cross-sectional area.

the Wiedemann–Franz law ($\kappa_e = L\sigma_e T$) is traditionally used to calculate κ_e, where $L = (\pi^2/3)(k_B/e)^2$ is normally applied for metals (e is the electron charge, and k_B is the Boltzmann constant). By contrast, in non-metals such as semiconductors and some minerals, the existence of a bandgap results in much smaller σ_e and, thus, smaller κ_e, making κ_e negligible compared with κ_l. Therefore, in this Review, we primarily discuss κ_l and denote it as κ.

Fourier's law describes how efficiently the heat can be conducted through a material from its high-temperature to low-temperature regions. However, in practical applications of hetero-materials, one should consider that, besides transport through the materials, heat must also be conducted across the interfaces of different materials (including dissimilar, epitaxial, bonded and contact interfaces). In this case, the thermal transport efficiency is commonly evaluated by the thermal resistance

$$R = \Delta T/q \tag{3}$$

where ΔT is the temperature difference between the two surfaces (with unit K) and q is the rate of conduction of thermal energy through the two surfaces (with unit W). Therefore, the total thermal resistance R consists of the thermal conduction part of the materials that is dependent on the κ and thickness of the materials, as well as the thermal boundary resistance (TBR) at the interface of two different materials. TBR normally results in an abrupt temperature drop at the hetero-materials interfaces, forming a significant bottleneck for the thermal transport. Mathematically, TBR is the inverse of ITC, which is normally expressed by the symbol of G (REF.[81]). On the one hand, ITC is a critical thermal parameter that governs the efficiency of thermal energy dissipation, and high ITC is desirable in a wide range of devices, such as high-power and high-frequency transistors, photodiodes, light-emitting diodes and phase-change memory devices[53,54,82–85]. On the other hand, low ITC also implies that the equivalent ultrathin interfacial material formed at the heterogeneous interface has low κ; this is desirable for applications in TE materials and thermal barrier coatings, among others[56,86–89]. All these applications require fundamental knowledge of ITC-related thermal-physical theories and progress to date has been be achieved by focusing investigations on its relationship with interfacial properties and the near-interface material properties[64,65,90–98] (FIG. 1b; Supplementary Information).

Application of extreme pressure can profoundly affect the phonon properties by changing the elastic constants, phonon velocities, phonon lifetimes, phonon densities of states, interfacial bonding stiffness, and so on. Many of these pressure-dependent phonon behaviours can be directly investigated by inelastic optical scattering. For example, the phonon velocities and elastic properties can be measured by in situ high-pressure Brillouin scattering techniques[39,99] and gigahertz ultrasonic interferometry techniques[100–103]. The pressure-dependent phonon dispersion and density of states can be measured by inelastic X-ray scattering techniques[104–106] and inelastic neutron scattering techniques[107–109].

These phonon behaviours are closely related to the phonon transport (and, thus, thermal transport) properties of materials. Upon compression, various pressure dependences of κ are reported, making the detailed mechanism of thermal transport modulated by pressure particularly complicated (FIG. 1c). In general, the pressure dependences of κ are classified into increasing, decreasing, independent and anomalous trends. Normally, κ increases dramatically under pressure, because the strain generated by pressure enhances the atomic interactions and compresses the bonds, thereby, modifying the phonon dispersions to greatly enhance the phonon velocities. Such an enhancement of κ is, in some cases, nonlinear. This nonlinearity is found to arise from the combined effects of decreased phonon relaxation time coupled with increased phonon group velocity[110]. Note that the κ_e discussed above largely depends on the σ_e and, thus, can have several orders of magnitude increase; however, it is still negligible compared with the value of κ_l in non-metals. However, κ can also decrease under pressure; such a decrease is thought to result from pressure-induced phonon anharmonicity and phonon softening[111]. First-principles calculations reveal that the decreased κ under pressure is mainly a result of the stronger third anharmonic interaction, the large mass ratio and the significant acoustic–optical frequency gap[112]. When κ is independent of pressure, this is currently thought to be caused by strong electronic correlation effects driven by the electronic topological transition[113].

As to the anomalous trend of κ, several mechanisms have been proposed. In the case of the anomalously decreased pressure dependence of κ for some materials, it is found that the intrinsic three-phonon scattering process contributes less than in other cases, due to the materials' large acoustic–optical frequency gap at high pressures, while more complicated scattering processes between acoustic phonons dominate and increase the overall phonon scattering[63]. In another case of non-monotonic behaviour, κ first increases and then decreases with increasing pressure. Possible mechanisms for this behaviour are the competing scattering processes of three-phonon and four-phonon interactions at high pressures[65] or the interplay between group velocity and phonon relaxation time under pressure[114]. In the case of the diverse pressure dependence of κ revealed in some rare-earth pyrochlores, the competition between the enhancement of phonon group velocity and the reduction of phonon relaxation time determines the pressure dependence[115].

Characterization methods

Thermal characterization techniques have been developed in apparatus such as piston–cylinder cells, multi-anvil cells and DACs, for both bulk and thin-film materials, and for both temperature-dependent and pressure-dependent measurements. The techniques are normally classified as steady-state or transient methods. Among the existing standard thermal characterization techniques, common steady-state methods for bulk materials are the absolute technique, comparative technique, radial heat flow method and parallel conductance method; for thin films, common methods are the steady-state electrical heating method and the Raman-based opto-thermal

method. Transient methods for bulk materials consist of the pulsed power technique, the hot-wire method and the transient plane source method; methods for thin films are the 3ω method, the laser flash method and the time-domain/frequency-domain thermoreflectance (TDTR/FDTR) method[116–131].

Only Raman-based opto-thermal, laser flash and TDTR/FDTR are optical methods, whereas the others are electrical methods that require complicated fabrication of heaters, sensors or thermocouples. The size of the electrical beads or pads is normally larger than the chamber size of the high-pressure apparatus, making these electrical-based high-pressure thermal characterization techniques challenging to perform. Piston–cylinder cells and multi-anvil cells are larger in size than the DAC, allowing more sample space for the thermocouple layout, but are normally limited at pressure range below 30 GPa (note that the multi-anvil cell is a commonly used first-order apparatus, with a wide sample space and a pressure limit <10 GPa)[10,132–135]. However, pressure of at least 20 GPa is usually needed to obtain ~50% increase in parameters such as the elastic constants that are relevant to thermophysical properties[99,136–139]. A DAC can generate much higher pressure exceeding 100 GPa, but the narrow space left between the anvils makes it extremely difficult to spread the wires, thermocouples and heaters.

In fact, the high-pressure thermal characterization methods have nearly 100 years of development (FIG. 1d). The main steady-state methods used in piston–cylinder pressure cells or multi-anvil cells[140] are the thermocouple and heater method[10,141–143] and the Ångström method[132,134,135,140,143–146] (FIG. 2a); in DACs, the main steady-state methods are the optical thermal grating method[147–149] (FIG. 2b), the thermocouple method[150] (FIG. 2c) and the Raman-based opto-thermal method[66,111,151,152] (FIG. 2d). Transient methods include the transient hot-wire method (FIG. 3a) for piston–cylinder cells[133,153–162], the pulsed heating method for multi-anvil cells[163,164] (FIG. 3b) and the TH method[17,47,48,165,166] (FIG. 3c; Supplementary Fig. 2) and the TDTR method[18,35,86,96,167–173] (FIG. 3d; Supplementary Fig. 3) for DACs. The optical contactless methods of the TH and TDTR techniques make it possible to investigate thermal properties at extremely high pressures. Here, we describe progress in the TH and TDTR techniques. Details of all high-pressure thermal characterization methods mentioned above are provided in the Supplementary Information.

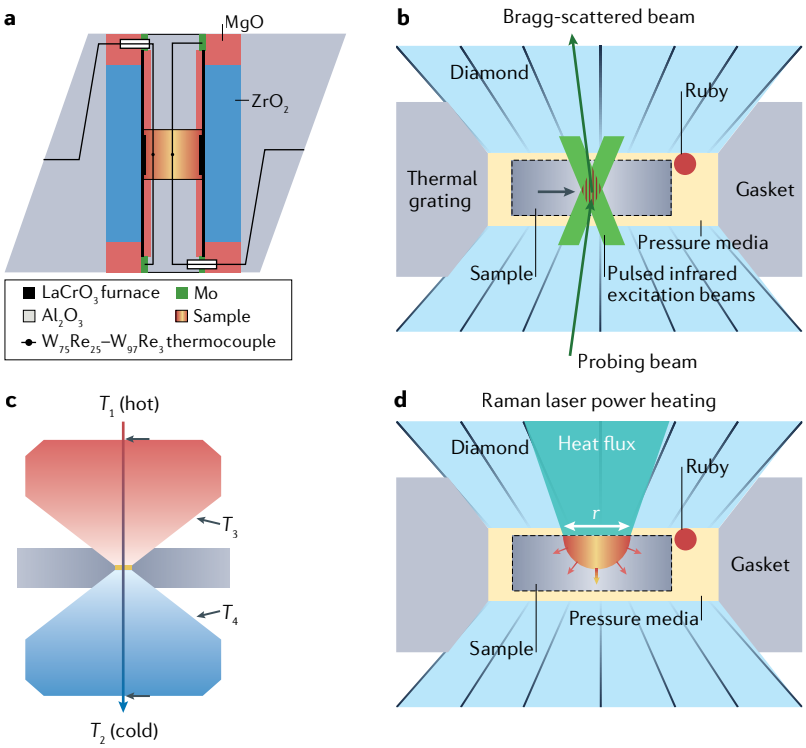

Fig. 2 | **Steady-state thermal characterization methodologies used under pressure.** **a** | The Ångström method developed in the multi-anvil cell[132]. **b** | The thermal grating method applied in a diamond anvil cell (DAC). **c** | The thermocouple method used in a DAC. T_1 and T_2, temperatures measured at the hot surface of the heating diamond anvil and at the cold surface of the heat-sinking diamond anvil, respectively; T_3 and T_4, temperatures measured near the culet of the hot anvil and the cold anvil, respectively. **d** | The Raman-based opto-thermal method used in a DAC[111]. *r* is the spot diameter of the excitation laser. Part **a** is adapted with permission from REF.[146], National Academy of Sciences. Part **b** is adapted with permission from REF.[149], Springer. Part **c** is adapted with permission from REF.[150], AIP.

TH method in DACs

In 2007, an optical contactless TH method (FIG. 3c; Supplementary Fig. 2) was developed in combination with the DAC techniques to measure the high-pressure, high-temperature thermal diffusivity of several minerals at pressures and temperatures as high as 125 GPa and 2,600 K (REFS[17,47,48,165,166]). More recently, this technique has been modified to enable measurements of metallic samples and to determine the κ of non-metallic samples with greater accuracy[174]. The TH method is currently one of the few methods appropriate for high-temperature, high-pressure measurements of thermal properties, especially for sample temperatures above 1,400 K. This method has been used to measure the κ of solid Fe at planetary core conditions of ~130 GPa and 3,000 K (REF.[47]) and, later, the κ of solid Fe and Fe–Si alloys up to 144 GPa and 3,300 K (REF.[48]), and the assemblage of lower-mantle minerals crystallized from pyrolite glass at temperatures up to 2,500 K at 120 GPa (REF.[175]).

TDTR method in DACs

TDTR is another contactless optical method that is widely applied to measure κ (REFS[86,167]) and ITC[96,168] in thin films. The TDTR method can provide an accuracy of 10–35% (depending on the pressure range) and a very fast measurement time. Moreover, the technique is readily compatible with DAC operation because the anvils are transparent for visible and near-infrared lasers that are normally used in TDTR. In 2009, the TDTR method was successfully combined with the DAC technique (that is, the TDTR-DAC technique) (FIG. 3d; Supplementary Fig. 3) to measure the pressure-dependent κ of muscovite mica up to 24 GPa (REF.[18]) and then the pressure evolutions of κ of materials from crystals to amorphous polymers up to 60 GPa. Later, to study how the extracted κ is affected by variations in the thermophysical parameters of metal film transducers at high pressures, the pressure evolutions

of critical thermal parameters (thermoreflectance, piezo-optical coefficient and physical stability) for several metal film transducers (Ta, Al and Au(Pd) thin films) were further investigated. The acoustic strengths for Ta and Au(Pd) films are essentially independent of pressure, whereas they drop abruptly and remain small for the commonly used Al film upon initial loading and up to 12 GPa (REF.[170]).

The TDTR-DAC technique has also been used to measure κ in liquids, as pressure-transmitting media such as methanol–ethanol mixture and silicone oil[171]. Furthermore, the ITC at heterointerfaces (such as Al/SiC, Al/graphene/SiO_x/SiC, Al/SiO_x/SiC) as a function of pressure can be extracted using this method[176]. Based on the TDTR-DAC technique, in 2019, this method was extended to combine with a picosecond-pulsed-laser-based transient thermoreflectance technique to measure the pressure-dependent cross-plane κ of MoS_2 up to 25 GPa (REFS[35,172]). Moreover, an in situ method was developed for measuring the high-pressure, high-temperature thermal diffusivities of Pt and Fe up to ~60 GPa and 2,000 K, and κ in post-perovskite up to 180 GPa and 1,560 K, by combining the thermoreflectance measurements (albeit with nanosecond laser pulses) and laser-heated DAC techniques[173,177].

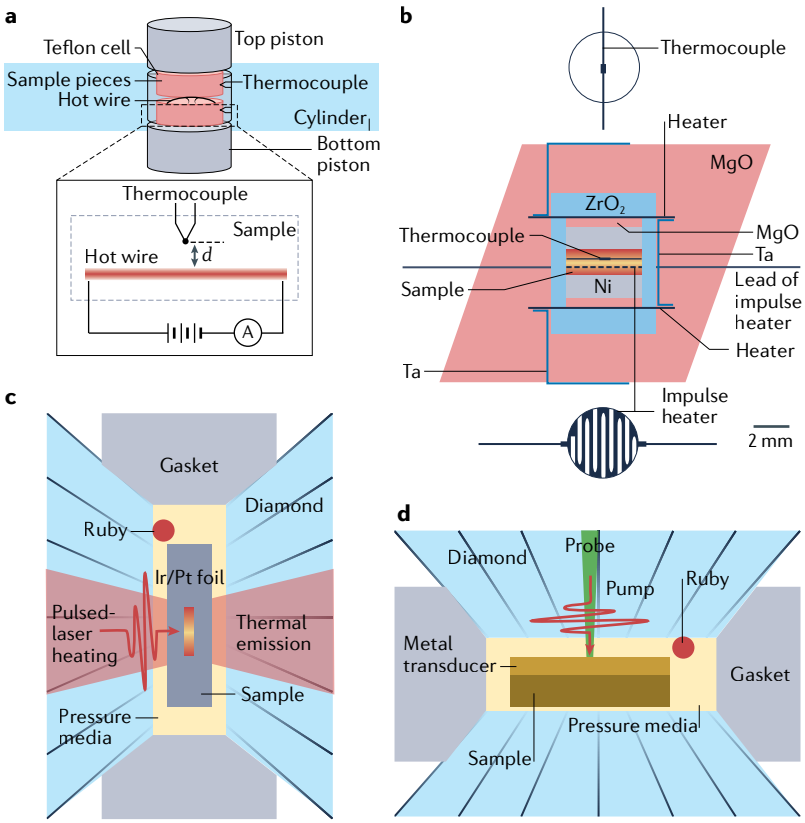

Fig. 3 | **Transient thermal characterization methodologies used under pressure.** **a** | The transient hot-wire method developed in the piston–cylinder cell. **b** | The pulsed heating method developed in the multi-anvil cell. **c** | The pulsed-laser transient heating method applied in a diamond anvil cell. **d** | The time-domain thermoreflectance method and picosecond transient thermoreflectance method applied in a diamond anvil cell. Part **a** is adapted with permission from REFS[159,162], Elsevier. Part **b** is adapted with permission from REF.[163], Elsevier. Part **d** is adapted with permission from REF.[35], APS.

Thermal conductivity under pressure

In terms of the magnitude of κ and functional applications, we arrange materials into the following groups: gases, liquids and solids, the last of which consists of TE materials, Earth materials and semiconductor materials. We do so because the κ values of these materials are, in general, distributed from low to high, spanning over almost all known magnitudes of κ.

Gases

We use 'gas' to refer to materials that are in the gas phase at ambient conditions. In general, the κ values of gases under pressure are noticeably smaller than those of solids. FIGURE 4a and TABLE 1 summarize the κ of several typical gases with respect to pressure. Around 1 GPa, most gases transform into liquids or solids, accompanied by a rapid increase in κ.

Limited by experimental techniques, the majority of the thermal studies of gases in the last century was within the pressure range of 1 GPa (REF.[67]). For instance, κ was measured in hydrogen using a coaxial cylindrical cell for pressure up to 66 MPa in 1966, and the effects of temperature on the κ of hydrogen under pressure were also established[178]. Furthermore, pressure-dependent κ parameters of oxygen, methane, nitrogen, neon, argon and other gases were also investigated, predominantly via the transient hot-wire method[179–183].

More recently, with the help of the DAC and TH techniques, the pressure range of thermal characterizations of gases has been extended over 10 GPa. In 2012, the κ of argon was measured in a pulsed-laser transiently heated DAC at pressures up to 50 GPa and temperatures up to 2,500 K (REF.[184]), paving the way for thermal studies of gases at higher pressures. For argon, κ at high pressures was predicted through first-principles-based phonon Boltzmann transport equation (BTE), density functional theory (DFT) and molecular dynamics methods[185,186], providing valuable guidance for experimental studies. The κ of argon increases rapidly by nearly four orders of magnitude when the pressure is increased to about 50 GPa (FIG. 4a). This trend is caused by argon rapidly crystallizing into a pure solid at a pressure of around 1 GPa; the κ of a crystal, in general, increases with pressure much faster than that of a gas, liquid or amorphous material.

Later, via DAC and pulsed-laser heating techniques, a planetary interior condition of about 140–170 GPa and 4,000 K was obtained. At these conditions, the κ of liquid metallic hydrogen, the most abundant material in the Solar System, was estimated to be 100–140 $Wm^{-1}K^{-1}$, based on the calculated electrical conductivity obtained from measured optical conductivity data using the Wiedemann–Franz law[187].

Liquids

Early studies on the κ parameters of liquids under pressure were limited to pressures of approximately 1 GPa and focused on organic liquids, such as oil, ethanol and toluene, to explore their implications on food and industrial products[188–190]. There was also interest in the pressure-dependent κ of pressure-transmitting media used in DACs[171], such as methanol–ethanol mixture

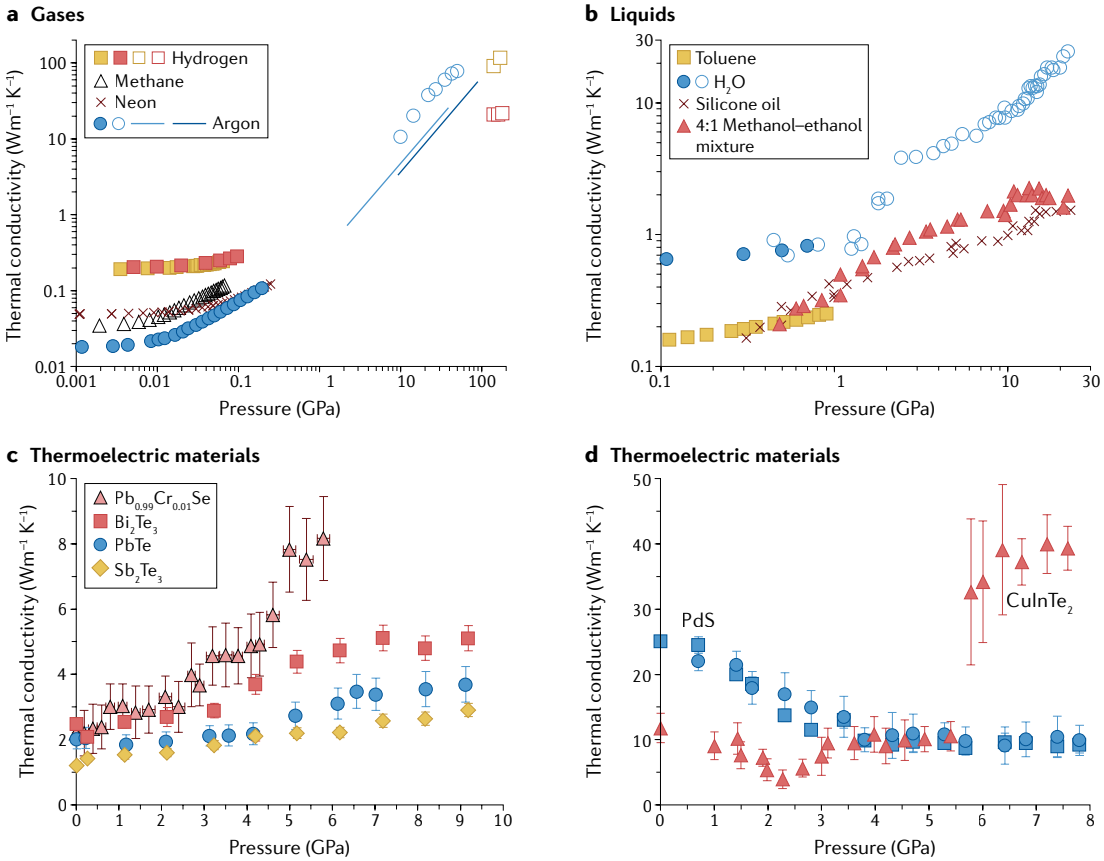

Fig. 4 | **Thermal conductivity of gases, liquids and thermoelectric materials under pressure. a** | Hydrogen, neon, argon and methane gases; lines are simulation results. Values are taken from REFS[178,180,182,184–187,257,259]. **b** | Liquids of H_2O, silicone oil, methanol–ethanol mixture and toluene. Values are taken from REFS[171,188,189,191]. **c**,**d** | Thermoelectric materials $Pb_{0.99}Cr_{0.01}Se$, Bi_2Te_3, PbTe and Sb_2Te_3 (part **c**) and PdS and $CuInTe_2$ (part **d**), all at 300 K. Values are taken from REFS[66,111,152,193,195].

and silicone oil. Measuring these parameters is essential for the accurate study of many important physical parameters, such as κ, of other materials under pressure. In addition, H_2O was also systematically studied[191,192]. Understanding the fundamental physical properties of H_2O, especially the κ of the Earth interior's environment, is important in exploring the origins of life. The evolution of κ of the above-mentioned liquids with pressure is plotted in FIG. 4b and summarized in TABLE 1, showing typical changes on the orders of 0.1–10 $Wm^{-1}K^{-1}$ within the transformation range from liquids to solids. Notably, the κ of H_2O (in its ice VII polymorph) appears to be an order of magnitude higher than that of silicone oil or 4:1 methanol–ethanol mixture at similar pressures above 20 GPa (FIG. 4b). This trend mainly arises from the fact that the κ of a crystal (such as water ice) typically increases rapidly with pressure, following approximately a $P^{3/2}$ dependence, whereas the κ of amorphous materials (such as silicone oil) increases relative slowly with pressure, following approximately a $P^{1/2}$ dependence.

Solids

Pressure dependence of the thermal transport in solids and amorphous materials has been studied for approximately 100 years. Here, based on the magnitude of materials' thermal conductivity ranging from low to high and the present research focus of materials' functions, we mainly discuss the pressure-dependent κ of solid materials in divisions of TE materials, Earth materials and semiconductor materials (FIGS 4–6; TABLE 1).

TE materials. TE materials with a high figure of merit (zT, which is normally expressed as $zT = \sigma S^2 T/\kappa$, where S is the Seebeck coefficient) are an ideal candidate to overcome the future energy crisis by transforming waste heat into power generation. According to their working temperatures, TE materials are normally classified as Bi_2Te_3-based low-temperature (<400 K), PbTe-based medium-temperature (600–900 K) and SiGe-based high-temperature (>900 K) divisions. The bottleneck is that the zT is still too low to achieve a value >3 for practical applications, despite much progress in the existing modulation methods, such as doping, alloying, temperature and nanostructure engineering. As mentioned above, pressure tuning can also be a promising and reliable approach to modulate the TE properties, by modifying physical and chemical properties even at room temperature, including σ and κ, ultimately achieving high zT values.

Bi_2Te_3 is a typical commercial, low-temperature TE material with a best zT value of around 1. When pressurized and electrically heated by contactless chromel wires to create temperature drops in a DAC, its κ increases from 2.47 $Wm^{-1}K^{-1}$ at ambient pressure to ~5.6 $Wm^{-1}K^{-1}$

Table 1 | **Summary of thermal conductivities for various materials from gases, liquids to solids investigated under pressure**

Materials	Strain type	Methods	Maximum pressure	Thermal conductivity ($Wm^{-1}K^{-1}$)	Ref.
Gases					
H_2	Comp.	–	0.066 GPa	0.19–0.24 (0.00354–0.0656 GPa, 298 K)	178
H_2	Comp.	Transient short hot-wire method	0.099 GPa	0.197–0.28 (0.00026–0.09776 GPa, 323 K)	257
N_2	Comp.	Transient hot-wire method	0.0277 GPa	0.038–0.046 (0.001–0.0277 GPa, 470 K)	258
O_2	Comp.	Transient hot-wire method	0.07 GPa	0.028–0.068 (0.002–0.0653 GPa, 310 K)	179
Ne	Comp.	Parallel-plate method	0.26 GPa	0.05–0.12 (1 atm–0.25 GPa, 298 K)	182
Ar	Comp.	Transient hot-wire method	0.011 GPa	0.018–0.021 (0.00058–0.00631 GPa, 308 K)	183
Ar	Comp.	Parallel-plate method	0.24 GPa	0.018–0.107 (1 atm–0.196 GPa, 298 K)	259
Ar	Comp.	Transient heating technique	50 GPa	10.66–78.28 (10–50 GPa, 300 K)	184
Ar	Comp. + tension	MD + BTE calculations	6% comp. + 6% tension	0.1–10 (isotropic strains from −0.06 to 0.06, 20 K)	260
Ar	Comp.	MD calculations	50 GPa	0.72–25.93 (0–50 GPa, 293 K)	185
Ar	Comp.	DFT + BTE calculations	150 GPa	3.32–56.71 (10–90 GPa, 400 K)	186
Methane	Comp.	Transient hot-wire method	0.07 GPa	0.0337–0.1169 (0.00099–0.0673 GPa, 295 K)	180
$N_2 + CO_2$	Comp.	Transient hot-wire method	0.03 GPa	Change with proportion	258
Liquids					
H_2O	Comp.	Line heat source probe	0.7 GPa	0.65–0.82 (0.108–0.7 GPa, 298 K)	188
H_2O	Comp.	Transient hot-wire method	0.8 GPa	0.56–1.54 (0–0.65 GPa, 273–243 K)	261
H_2O	Comp.	TDTR + DAC	22 GPa	0.54–24.69 (0–22 GPa, 300 K)	191
4:1 Methanol–ethanol	Comp.	TDTR + DAC	23 GPa	0.21–1.98 (0–23 GPa, 300 K)	171
Silicone oil	Comp.	TDTR + DAC	23 GPa	0.16–1.53 (0–23 GPa, 300 K)	171
Toluene	Comp.	ac-Heated-wire method	1 GPa	0.128–0.25 (0–0.9026 GPa, 300 K)	189
Thermoelectric materials					
Bi_2Te_3	Comp.	Electrical heating	10 GPa	2.47–5.6 (0–10 GPa, 300 K)	193
Sb_2Te_3	Comp.	Electrical heating	10 GPa	1.22–3 (0–10 GPa, 300 K)	193
PbTe	Comp.	Electrical heating	11 GPa	2–4 (0–11 GPa, 300 K)	195
PdS	Comp.	Opto-thermal Raman	10 GPa	25–9 (0–10 GPa, 300 K)	152
$Pb_{0.99}Cr_{0.01}Se$	Comp.	Opto-thermal Raman	6 GPa	2.1–8.2 (0–6 GPa, 300 K)	66
$CuInTe_2$	Comp.	BTE calculations	5 GPa	7.5–4.1 (0–5 GPa, 300 K)	262
$CuInTe_2$	Comp.	Opto-thermal Raman	8 GPa	2.1–8.2 (0–8 GPa, 300 K)	111
Earth materials					
Iron	Comp.	TDTR + DAC	120 GPa	76–120 (0–120 GPa, 300 K)	48
Iron	Comp.	TH + DAC	130 GPa	20–40 (35–130 GPa, 2,000–3,000 K)	47
Iron (hexagonal close-packed)	Comp.	TH + DAC	134 GPa	70–80 (constant above 46 GPa)	113
Iron	Comp.	DFT calculations	340 GPa	150–250 (120–340 GPa, 4,500–6,500 K)	205
$Fe_{0.96}Si_{0.04}$	Comp.	TDTR + DAC	125 GPa	16.5–60 (0–125 GPa, 300–3300 K)	48

Table 1 (cont.) | **Summary of thermal conductivities for various materials from gases, liquids to solids investigated under pressure**

Materials	Strain type	Methods	Maximum pressure	Thermal conductivity ($Wm^{-1}K^{-1}$)	Ref.
Earth materials (cont.)					
$Fe_{0.85}Si_{0.15}$	Comp.	TDTR + DAC	144 GPa	11.5–40 (0–144 GPa, 300–3,300 K)	48
MgO	Comp.	TDTR + DAC	60 GPa	53–161 (0–60 GPa, 300 K)	218
MgO	Comp.	DFT + PBTE calculations	150 GPa	66–341 (0–150 GPa, 300 K); 2–46 (0–150 GPa, 3,000 K)	212
(Mg, Fe)O	Comp.	TDTR + DAC	120 GPa	2.8–50 (0–120 GPa, 300 K)	221
$MgSiO_3$	Comp.	TDTR (two sided) + DAC	144 GPa	8–37.1 (11–144 GPa, 300 K)	229
$(Mg, Fe)SiO_3$	Comp.	TDTR + DAC	120 GPa	5–30 (0–120 GPa, 300 K)	222
(Mg, Fe)O; $(Mg, Fe)SiO_3$	Comp.	TH + DAC	133 GPa	6–11 (0–133 GPa, 300–2,800 K)	165
Ringwoodite	Comp.	TDTR + DAC	25 GPa	3–16 (0–25 GPa, 300 K)	228
$(Mg, Fe)CO_3$	Comp.	TDTR + DAC	67 GPa	2.5–45 (0–67 GPa, 300 K)	223
Pyrolite	Comp.	TH + DAC	124 GPa	3.9 (0–80 GPa, 2,000–2,500 K); 5.9 (0–124 GPa, 2,000–3,000 K)	175
Muscovite	Comp.	TDTR + DAC	24 GPa	0.46–6.6 (0–24 GPa, 300 K)	18
δ-(Al,Fe)OOH	Comp.	TDTR + DAC	110 GPa	5–60 (0–110 GPa, 300 K)	224
Semiconductor materials					
Si	Torsion	TDTR + DAC	24 GPa	142–7.6 (0–24 GPa, 300 K)	263
Si	Comp.	TDTR + DAC	45 GPa	73–300 (0–36 GPa)	239
Si	Comp. + tension	MD + BTE calculations	3% comp. + 3% tension	135–155 (isotropic strains from −0.03 to 0.03, 300 K)	260
Si	Comp. + tension	MD calculations	4% comp. + 4% tension	100–450 (Stillinger–Weber Si potentials, 300 K)	264
$Si_{0.991}Ge_{0.009}$	Comp.	TDTR + DAC	45 GPa	24–360 (0–36 GPa)	239
CuCl	Comp.	Transient hot-wire method	2.7 GPa	0.8–0.6 (0.5–2.7 GPa, 295 K)	241
GaAs	Comp.	DFT + BTE calculations	20 GPa	49–70 (0–16 GPa, 300 K)	110
BAs	Comp.	DFT + BTE calculations	80 GPa	1331–823 (0–80 GPa, 300 K)	65
MoS_2	Comp.	ps-TTR + DAC	19 GPa	3.5–25 (0–19 GPa, 300 K)	35
Monolayer silicene	Comp.	DFT + BTE calculations	10%	25–170 (0–10% strain, 300 K)	265
Monolayer h-BAs	Tension	MD calculations	3–7%	180.2–375 (3% strain along armchair direction); 180.2–406.2 (3% strain along zigzag direction)	251

BTE, Boltzmann transport equation; Comp., compression; DAC, diamond anvil cell; DFT, density functional theory; MD, molecular dynamics; PBTE, Peierls–Boltzmann transport equation; TDTR, time-domain thermoreflectance; TH, pulsed-laser transient heating; TTR, transient thermoreflectance.

at 10 GPa (FIG. 4c). However, its zT value decreases drastically at pressures above 3 GPa (REF.[193]). First-principles calculations indicate that the κ of Bi_2Te_3 reduces by 50% when under a 6% tensile strain and increases by 61% under a 4% compressive strain[194]. Using the same experimental high-pressure thermal characterization method as that in Bi_2Te_3, the κ of another commonly studied low-temperature TE material, Sb_2Te_3, was reported to increase from 1.22 $Wm^{-1}K^{-1}$ to ~3 $Wm^{-1}K^{-1}$ at ~10 GPa (FIG. 4c). By contrast, a nearly pressure-independent zT value was reported in Sb_2Te_3 (REF.[193]).

Among the medium-temperature TE materials, the pressure dependence of κ was measured through the DAC combined Raman opto-thermal method in a pressurized TE material of $CuInTe_2$ (REF.[111]). κ reduces from 11.7 $Wm^{-1}K^{-1}$ to a minimum of 4.1 $Wm^{-1}K^{-1}$ at 2.2 GPa. At pressures above 6 GPa, at which the material undergoes a transition into a new phase, κ jumps to ~30 $Wm^{-1}K^{-1}$ and keeps increasing to ~40 $Wm^{-1}K^{-1}$ at 7.9 GPa, where all the Raman modes almost vanish (FIG. 4d). Pressure-induced phonon anharmonicity and phonon softening are thought as the main mechanisms for such a reduction of κ under pressure. It is interesting that the κ of another TE material, PdS, continuously decreases from ~25 $Wm^{-1}K^{-1}$ at ambient pressure to ~9 $Wm^{-1}K^{-1}$ near 4 GPa and then saturates until ~11 GPa (REF.[152]) (FIG. 4d). A continuous decrease of κ is also witnessed in a half-Heusler TE material FeNbSb, in

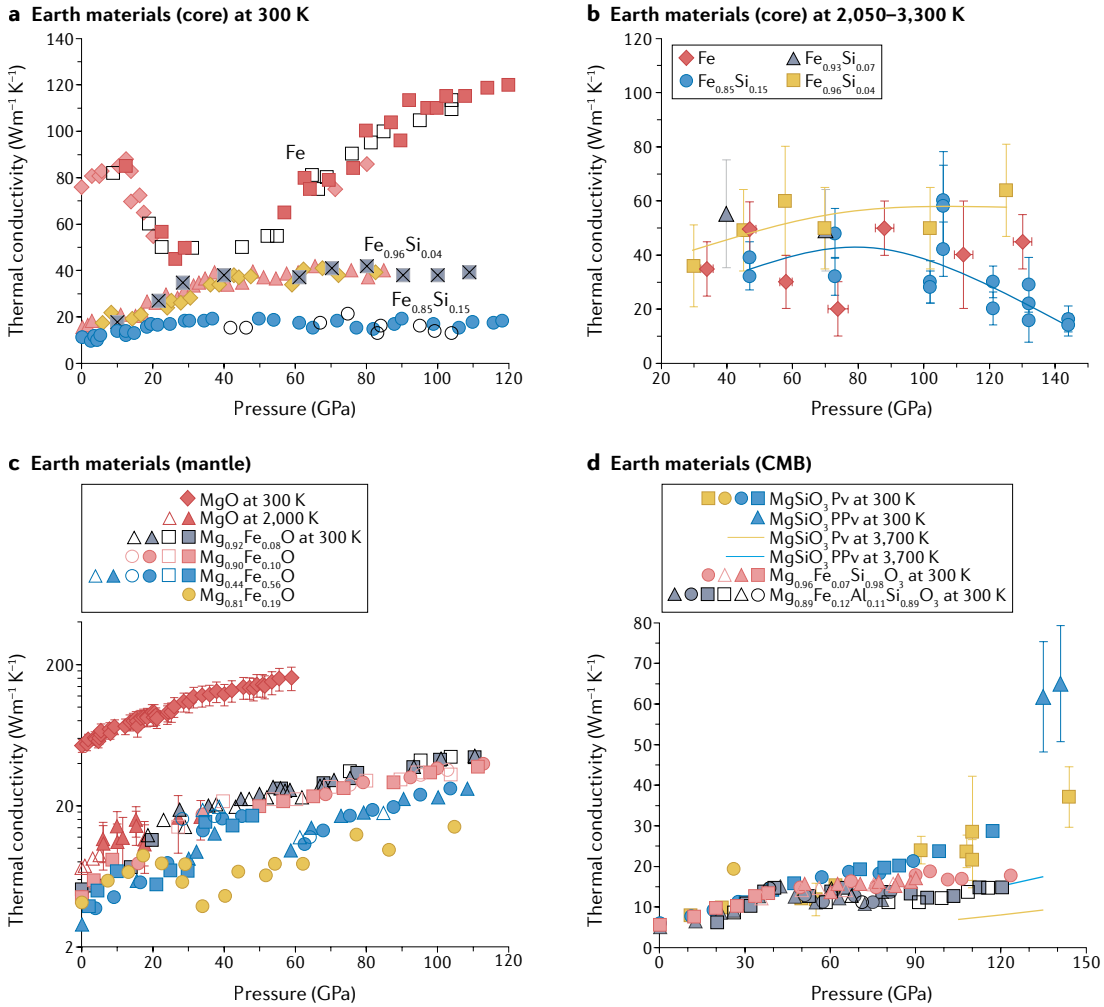

Fig. 5 | **Thermal conductivity of Earth materials under pressure. a** | Earth core materials of iron and iron–silicon alloys up to 120 GPa at 300 K. **b** | Earth core materials of iron and iron–silicon alloys up to 144 GPa and 3,300 K. The values are taken from REFS[47,48]. The lines are to guide the eye. **c** | Earth mantle materials for typical minerals of MgO and (Mg, Fe)O. The values are taken from REFS[17,165,218,221]. **d** | Earth materials for typical core–mantle boundary (CMB) minerals of $MgSiO_3$, (Mg, Fe)SiO_3 and (Mg, Fe, Al)SiO_3 up to 144 GPa and 3,700 K. The values are taken from REFS[222,229]. PPv, post-perovskite; Pv, perovskite.

which κ decreases from ~5 $Wm^{-1} K^{-1}$ at ambient pressure to ~2 $Wm^{-1} K^{-1}$ at 18 GPa (REF.[151]). An enhanced room-temperature zT value of ~1.7 (~4 times enhancement) was reported at ~2.8 GPa in a Cr-doped PbSe; this enhancement was ascribed to a pressure-driven topological phase transition at 2.6 GPa (REF.[66]). In this work, via a similar Raman opto-thermal method, an increase of κ from ~2 $Wm^{-1} K^{-1}$ at ambient conditions to ~6 $Wm^{-1} K^{-1}$ at 4.8 GPa was observed, followed by an immediate jump to a larger value of ~8 $Wm^{-1} K^{-1}$ due to the transition into a *Pnma* phase (FIG. 4c). For comparison, the high-pressure TE performance was also reported in its counterpart TE material of PbTe. Unlike that of Cr-doped PbSe, the κ of PbTe increases from 2 $Wm^{-1} K^{-1}$ to ~4 $Wm^{-1} K^{-1}$ within 11 GPa (REFS[195–197]) (FIG. 4c). Moreover, in another two typical medium-temperature TE materials, skutterudites $CoSb_3$ and $IrSb_3$, similar calculations to those used for Bi_2Te_3 show that the κ values of both exhibit an approximate parabolic trend with respect to pressure at the same temperature[198]. $CoSb_3$ has an increased κ from ~11.3 $Wm^{-1} K^{-1}$ at ambient conditions to ~13.3 $Wm^{-1} K^{-1}$ at 58 GPa with the maximum zT value, despite the largest κ of ~18.6 $Wm^{-1} K^{-1}$ appearing at ~30 GPa. However, $IrSb_3$ shows a decreased κ from ~14.2 $Wm^{-1} K^{-1}$ at ambient conditions to ~8.8 $Wm^{-1} K^{-1}$ at 54 GPa with the maximum zT value, but having the largest value of ~25.4 $Wm^{-1} K^{-1}$ at ~20 GPa.

Earth materials. Understanding the heat transport and thermal evolution of the Earth's interior requires knowledge of the thermal-physical properties of minerals and melts at relevant extreme temperatures and pressures. Several decades ago, there were a number of limitations on the direct measurements of thermal-physical parameters. To address this problem, pressure dependence of the Grüneisen parameter is commonly used to investigate the geophysics, as it reflects the measured changes in temperature associated with adiabatic compression. The Grüneisen parameter is, therefore, important in the calculation of Earth's adiabatic gradient to

understand the core convection and the Earth's geomagnetic field[199–204]. A large Grüneisen parameter normally indicates low κ, but this relationship is hard to be quantitatively and accurately correlated, especially at high temperature.

Developments in DAC techniques enable the κ of materials to be measured at high pressure and temperature. In the Earth's core, the κ values of core materials in high-pressure, high-temperature conditions directly determine the adiabatic heat flux, thermal and compositional energy that support the operation of the Earth's magnetic field. Meanwhile, κ of the Earth's lower-mantle minerals impacts mantle convection and affects the heat conduction from the core to the mantle. Conduction is the major heat transfer mechanism at the core–mantle boundary (CMB) and the magnitude of heat flux transfers from the core is determined by κ of the bottom boundary layer of the mantle. More importantly, this κ value of the bottom mantle boundary layer is intimately related to the instability of the boundary layer, the formation of mantle plumes, the long-term thermal evolution of both the mantle and the core, and the driving force for the generation of the geomagnetic field.

The Earth's core is composed of iron alloyed with some light elements. Iron is a major constituent of the Earth's core, thus, the κ of Fe and its alloys have been theoretically predicted at core conditions[205]. Experimentally, the κ of solid Fe, which is 18–44 $Wm^{-1}K^{-1}$ at pressures (130 GPa) and temperatures (3,000 K) of the core, was directly measured using a dynamically double-sided, infrared, continuous-wave, laser-heated DAC with one-side additional thermal disturbance created by another infrared pulsed laser[47,174,206]. At pressures and temperatures close to the outer core conditions, that is, 105 GPa and 3,300 K, the κ for solid Fe and liquid Fe was measured to be 46 ± 14 $Wm^{-1}K^{-1}$ and 42 ± 12 $Wm^{-1}K^{-1}$, respectively. These κ values were extracted from the resistivity values via the Wiedemann–Franz law using an ambient Lorenz number[207]. More recently, an increased κ of γ-Fe (90–125 $Wm^{-1}K^{-1}$) and a mixed phase of Fe (45–65 $Wm^{-1}K^{-1}$) with increasing pressure up to ~46 GPa was measured through a single-sided, laser-heated DAC technique, where the power absorbed by an Fe metal foil was calculated from a thermodynamic simulation in COMSOL[113]. For ε-Fe, κ is 70–80 $Wm^{-1}K^{-1}$ at 1,600–2,100 K (with an error of ~40%) and is almost

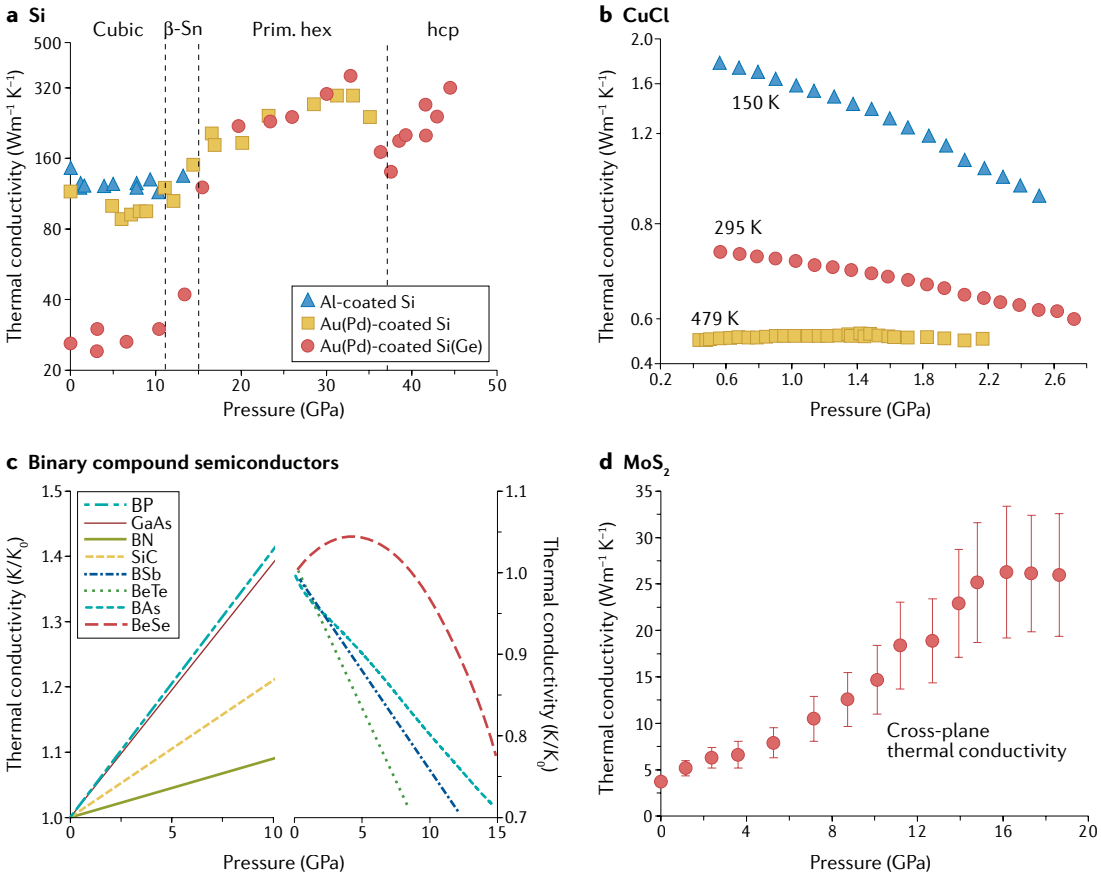

Fig. 6 | **Thermal conductivity of semiconducting electronic materials under pressure. a** | Semiconductor materials of Si and $Si_{0.991}Ge_{0.009}$ measured using time-domain thermoreflectance near 300 K at pressures up to 45 GPa. **b** | Wide-bandgap CuCl measured using the transient hot-wire technique within the pressure range 0.5–2.7 GPa and temperature range 100–480 K (REF.[241]). **c** | Normalized thermal conductivity calculated from first principles for binary compound semiconductors of GaAs, SiC, BP and BN with an increasing trend; BAs, BeTe and BSb with a decreasing trend; and BeSe with a non-monotonic trend. **d** | Thermal conductivity of the 2D material MoS_2. hcp, hexagonal close-packed; Prim. hex, primitive hexagonal. Part **a** is adapted with permission from REF.[239], APS. Part **c** is adapted with permission from REF.[63], APS. Part **d** is adapted with permission from REF.[35], APS.

independent of pressure up to 134 GPa; this pressure-independent κ of ε-Fe was attributed to the strong electronic correlation effects driven by the electronic topological transition[113].

The high-pressure κ values of solid Fe and Fe–Si alloys have been measured at both room temperature and high temperature up to 144 GPa and 3,300 K by the combination of TDTR[18] and TH methods[17,47]. At room temperature, the κ of solid Fe increases from ~76 $Wm^{-1}K^{-1}$ to ~90 $Wm^{-1}K^{-1}$ at ~13 GPa and then decreases to a minimum of ~40 $Wm^{-1}K^{-1}$ at ~40 GPa, followed by a further increase again, reaching ~130 $Wm^{-1}K^{-1}$ when the pressure is near the CMB condition (120 GPa); this minimum may be due to an electronic topological transition occurring at ~40 GPa (REF.[48]). The addition of Si impurities significantly lowers the κ of pure Fe. For example, at ambient conditions, $Fe_{0.96}Si_{0.04}$ has $\kappa = 16.5$ $Wm^{-1}K^{-1}$ and $Fe_{0.85}Si_{0.15}$ has $\kappa = 11.5$ $Wm^{-1}K^{-1}$. With increasing pressure, the κ values of both $Fe_{0.96}Si_{0.04}$ and $Fe_{0.85}Si_{0.15}$ increase monotonically up to 40 GPa and then saturate at ~40 $Wm^{-1}K^{-1}$ and 19 $Wm^{-1}K^{-1}$, respectively (FIG. 5a). However, at temperatures of ~3,300 K, the κ of $Fe_{0.85}Si_{0.15}$ first increases to ~40 $Wm^{-1}K^{-1}$ (80 GPa) and then decreases to ~20 $Wm^{-1}K^{-1}$ (144 GPa), whereas the κ of $Fe_{0.96}Si_{0.04}$ increases to ~60 $Wm^{-1}K^{-1}$ (125 GPa)[48] (FIG. 5b). All of these κ values measured by experimental methods are several times lower than those obtained by calculations and electrical resistivity measurements[205,208–211].

MgO is recognized as a typical mineral of lower-mantle materials. The κ of MgO has been calculated through a numerical technique that combines DFT and the Peierls–BTE method, providing a model for the pressure–temperature dependence of the κ of MgO at conditions from ambient to the CMB[212,213]. κ increases from 15–20 $Wm^{-1}K^{-1}$ at 24 GPa (the pressure of the 670-km seismic discontinuity) to 40–50 $Wm^{-1}K^{-1}$ at 135 GPa (the CMB pressure). Furthermore, at 2,000 K, the κ of MgO measured via the TH technique was found to have ~50% enhancement when increasing the pressure from ambient conditions to 32 GPa. In addition, the radiative part of κ of the lower mantle increases with depth until saturating at ~0.54 $Wm^{-1}K^{-1}$ at the depth of the CMB[17,165,214–217]. However, at 300 K, through TDTR measurements in DACs, the κ of MgO was found to increase from 50 $Wm^{-1}K^{-1}$ at ambient conditions to about 160 $Wm^{-1}K^{-1}$ at 60 GPa (REF.[218]) (FIG. 5c), agreeing well with the previous model and first-principles predictions[212,219,220].

Concerning other Earth minerals, recent investigations on the pressure dependences of the κ of other lower-mantle minerals include (Mg,Fe)O (REF.[221]) (Fe,Mg)SiO_3 (REF.[222]), $(Fe_{0.78}Mg_{0.22})CO_3$ (REF.[223]), δ-(Al,Fe)OOH (REF.[224]), $Mg_{0.94}Fe_{0.06}SiO_3$ (REF.[225]), $(Mg_{0.9}Fe_{0.1})O$ (REF.[225]), $Mg(OH)_2$ (REF.[226]), $CaGeO_3$ (REF.[140]), $(Mg_{0.9}Fe_{0.1})_2SiO_4$ (REF.[68]), olivine $(Mg_{0.9}Fe_{0.1})_2SiO_4$ (REF.[227]) and ringwoodite[228]. Among them, thermal anomalies were found in an important water-carrying mineral, δ-(Al,Fe)OOH, of which the κ varies 2–3-fold upon compression across the spin transition of iron, thus, leading to an abnormally low κ value at the lowermost pressure of the mantle[224]. Similar anomalous κ dependence was also observed in the mineral of $(Fe_{0.78}Mg_{0.22})CO_3$ when pressurized across the spin transition[223].

As an important mineral in Earth's lower mantle near the CMB, $MgSiO_3$ has κ ~37.1 $Wm^{-1}K^{-1}$ at 144 GPa, nearly six times higher than that at ambient conditions, as measured by a modified TDTR technique in which the pump and probe lasers illuminate the opposite sides of the sample of the DAC[229] (FIG. 5d). Through non-equilibrium molecular dynamics simulations, the κ values of $MgSiO_3$ at 1,000 K show enhancements from 8.5 $Wm^{-1}K^{-1}$ to 14–20 $Wm^{-1}K^{-1}$ in the range of 20–130 GPa with an obvious anisotropy. Note that these recently measured and calculated values are within the range of previous estimates of κ values at the CMB (4–29 $Wm^{-1}K^{-1}$)[175,221,222,229–238].

Semiconductor materials. Enhancing the κ of semiconductor materials is a key for better thermal dissipation and thermal management in devices. To date, the majority of works on the pressure dependence of κ in semiconductor materials are first-principles calculations. For example, by separately calculating the harmonic and anharmonic effects of strain on materials stiffness and phonon properties, the κ of the widely used Si is found to be constant within a 3% compression (equivalent to ~4 GPa) and has only about a 10% decrease when it is under a 3% tension; this weak strain dependence was mainly ascribed to the anomalous increase of the phonon lifetime with the strain when moving from compression to tension and the greater root-mean-square displacement allowed under compression. Experimentally, a κ of Si without obvious pressure dependence within the entire cubic phase range of 0–13 GPa was measured via TDTR, whereas a continuously increased κ to ~300 $Wm^{-1}K^{-1}$ was witnessed within the metallic phase in the range of 16–36 GPa (REF.[239]) (FIG. 6a). Meanwhile, the κ of $Si_{0.991}Ge_{0.009}$ increases with pressure in both the semiconducting phase and the metallic phase, but exhibits a jump between the cubic phase and the primitive hexagonal phase at ~13 GPa and a sharp drop between the primitive hexagonal phase and the hexagonal close-packed phase at ~36 GPa (REF.[239]).

Diamond has the natural highest κ among the known semiconductors, making it valuable as an ultrawide-bandgap semiconductor. A dramatically increased κ of ~12,000 $Wm^{-1}K^{-1}$ for natural diamond (~17,000 $Wm^{-1}K^{-1}$ for isotope-pure diamond) at room temperature and 400 GPa was predicted using density functional perturbation theory combined with the phonon Boltzmann equation[240]. The pressure-induced enhancement of the frequency scale results in the relatively high acoustic velocities and low phonon–phonon scattering rates. These are regarded as the primary mechanism for the enhanced κ upon compression. Within this framework, the increase of the optical mode frequencies with pressure weakens the acoustic–optical coupling, thus, driving the κ of diamond to extremely high values[240].

Anomalous pressure dependences of κ were reported in some compound semiconductors, especially those of large mass ratio. For example, using a transient hot-wire technique, the κ of the wide-bandgap semiconductor CuCl was experimentally measured to decrease continuously from 0.5 to 2.7 GPa and from 100 to 480 K (REF.[241]) (FIG. 6b). This typical decrease in κ with increasing pressure

was found to correlate with large and negative Grüneisen parameters (~2.5) for the transverse-acoustic phonons. It is also found that the atomic mass ratio of CuCl is as large as 1.8, resulting in the optic and acoustic modes being well separated[241–243]. In addition, the pressure dependence of κ of several binary compounds with various mass ratios has been examined using a first-principles approach[63]. The calculations revealed that those compounds with similar mass ratio, such as GaAs, SiC, BN and BP, show an increased κ with pressure, whereas compounds with large mass ratio (such as BSb, BAs, BeTe and BeSe) that have significant frequency gaps between the acoustic and optical phonons exhibit a decreasing κ with pressure[63] (FIG. 6c). These anomalous pressure dependences were found to arise from the fundamentally different scattering processes of acoustic phonons.

Future developments of electronics require significant shrinking of semiconductors, especially in their thickness. Beyond meeting the needs of advanced technologies and new device layouts, the naturally ultrathin and uniform 2D semiconducting materials also demonstrate potential for applications in next-generation nanoelectronics. These materials normally possess highly anisotropic κ along the in-plane and cross-plane directions due to their weak interlayer bonding by van der Waals forces. For example, the reported in-plane κ ($\kappa_{\parallel}$, ranging from 35 to 85 $Wm^{-1}K^{-1}$ at ambient conditions) of MoS_2 (REFS[244–246]), an archetypal transition metal dichalcogenide (TMD) with a layered crystal structure, is more than ten times larger than the cross-plane κ ($\kappa_{\perp}$ ~2–4.5 $Wm^{-1}K^{-1}$)[244,247,248]. Small $\kappa_{\perp}$ could jeopardize heat dissipation of TMD-based electronics. Strain engineering and pressure engineering are promising to enhance and modulate $\kappa_{\perp}$, which can also revolutionize the thermal management techniques in all TMD-based electronic devices. Despite extensive theoretical studies of the effect of strain on κ in TMDs, no consistent conclusions have been drawn[61,69,249,250]. In bulk MoS_2, $\kappa_{\perp}$ increases from 3.5 $Wm^{-1}K^{-1}$ at ambient conditions to ~25 $Wm^{-1}K^{-1}$ at ~25 GPa, as observed using a picosecond transient thermoreflectance technique[35] (FIG. 6d). Combined with coherent phonon spectroscopy and first-principles calculations, it was further revealed that the notable enhancement in $\kappa_{\perp}$ arises from the strain-enhanced interlayer interaction, heavily modifying the phonon dispersion curves and decreasing the phonon lifetime. Note that an abnormal strain dependence has been shown in a hexagonal phase monolayer BAs system. Through DFT–BTE calculations, the $\kappa_{\parallel}$ was predicted to be enhanced from 180.2 $Wm^{-1}K^{-1}$ to 375.0 $Wm^{-1}K^{-1}$ and 406.2 $Wm^{-1}K^{-1}$ along the armchair and zigzag directions, respectively, under only 3% stretching[251]. This enhancement is correlated to the fact that stretching makes the flexural out-of-plane mode the dominant heat carrier.

DAC simulations of materials in the Earth's interior

The Earth's core is under extreme conditions, with temperature ~6,000 K and pressure over 360 GPa at its centre. Laser-heated DAC techniques provide the necessary and effective approaches for studying the Earth's interior by providing the relevant pressure–temperature conditions. A variety of in situ probes coupled to DACs, such as X-ray diffraction, X-ray absorption and Raman spectroscopy, TH and TDTR[252–254], enable multiple experiments on geological materials, such as the core and the mantle minerals, to study their physical and chemical properties, thereby, contributing to understanding of the Earth's interior structure, composition and evolution.

Understanding heat transport is crucial to clarify the thermal evolution and dynamics of the Earth's interior. A wealth of exploratory works have been reported on the κ of materials present in the Earth's core, mantle and CMB, through DAC experiments at the high-pressure, high-temperature conditions of Earth and first-principles calculations[47,166,175,205,208,211,225]. Computing the thermal and electrical conductivity in liquid mixtures at the Earth's core conditions using first-principles calculations gives the adiabatic heat flux at the CMB of 8–16 TW. This value is higher than previous estimates, which are based on the mantle convection[205,255,256]. Experimentally, the κ of iron–silicon alloys at the Earth's core conditions was measured to be as low as 20 $Wm^{-1}K^{-1}$ through TDTR and TH experiments in DACs, suggesting a minimum heat flow of about 3 TW actually across the CMB, lower than previously expected[48]. In addition, the κ of solid iron at the Earth's core conditions was measured using laser-heated DACs to be 18–44 $Wm^{-1}K^{-1}$; these values are near the low end of previous estimates and are in agreement with palaeomagnetic measurements, indicating that the solid inner core has persisted since the beginning of Earth's history and is as old as the dynamo[47]. Moreover, the κ of mantle minerals measured in a DAC near the conditions of the lowermost mantle gave a value of ~3.9 $Wm^{-1}K^{-1}$ at 80 GPa and 2,000–2,500 K, and ~5.9 $Wm^{-1}K^{-1}$ at 124 GPa and 2,000–3,000 K (REF.[175]). These results further indicate that high-pressure, high-temperature experiments and simulations of Earth materials are important in the exploration of Earth's geodynamo and the understanding of Earth's evolution.

Outlook

To date, one of the greatest challenges for characterizing κ under pressure is that the samples loaded in the high-pressure apparatus are normally very small. For example, in the contact method using thermocouples and heaters, the sample size needs to be larger than the thermocouple, pushing the limited space within the DAC. Similarly, in contactless methods that use optics, the sample size needs to be larger than the spot radius of the pump laser used in TDTR and TH methods or the excitation laser used in the Raman opto-thermal method. In addition, optical methods require the samples' surfaces to be as smooth as possible, otherwise the optical signal would be degraded by scattering. Another challenge is the measurement of the in-plane κ under pressure or the anisotropic evolution of κ under pressure. Despite many studies on the pressure-dependent κ, the outcomes are either isotropic or cross-plane κ, whereas high-pressure measurements on the in-plane κ of anisotropic materials are yet to be achieved. The in-plane κ has broad theoretical use and practical applications in many anisotropic materials, such as 2D materials and ultrathin films that are needed for lateral heat

spreading in electronics. Significant interest would be further raised if in-plane κ modulation can be definitively realized and theoretically understood through methods of the strain modulation.

Furthermore, κ modulation via strain may steer new directions in the development of electronics and devices for thermal management. Especially, but not limited to electronic systems, the intensity of heat density generation and the associated heat dissipation need to be fully understood and carefully conducted away, else the electronics will face significant temperature rise, leading to reliability challenges and possible failures. Take as an example transistors, at the heart of the electronics industry. The tendency described by Moore's law is related to successive shrinking of the device size to integrate a greater number of transistors onto a more compact chip, thus, leading to dramatic power consumption increase in the integrated circuits; this brings about a huge challenge in heat dissipation to ensure the device's high performance and reliability. For instance, the heat flux generated at the local hotspot due to self-heating during the operation can exceed 1,000 W cm^{-2} in high-electron-mobility transistors; this heat flux is a threat for device reliability and lifetime. From the viewpoint of thermal management, the total thermal resistance of devices needs to be minimized. This thermal resistance consists of the contributions from the κ and the thickness of materials, as well as the major hindrances of ITC. It should be noted that, in high-power transistors, we expect larger κ, whereas in thermoelectrics, lower κ values are desired. These contradictory details should be considered in thermal management design, and it is necessary to carefully consider the device purposes and requirements. In any case, both types of device applications would benefit from higher ITC to quickly and efficiently conduct heat across interfaces. Currently, enhancing the κ and the ITC of materials is achieved mainly by improving the materials quality with fewer defects and less grain boundary scattering, introducing high κ interfacial materials or fabricating smoother interfaces. Besides the above ambient methods, strain or pressure can also be used to enhance the κ of materials and the ITC at interfaces, although this research is still in early stages due to the challenges of high-pressure thermal characterization techniques; however, this method may inform new thermal management techniques in electronic devices.

An additional viewpoint worth noting is that improving the reliability and precision in determining the pressure-dependent thermophysical properties requires further implementation of advanced characterization techniques. Currently, defying the small size and very narrow space of DAC tools, all-optical fast laser thermoreflectance, transient heating and opto-thermal contactless experimental techniques have attracted more and more interest, and displayed great potential in future developments, although there are still many unknowns that need to be explored and improved in these methods.

Published online 21 February 2022

1. Mao, H.-K., Chen, X.-J., Ding, Y., Li, B. & Wang, L. Solids, liquids, and gases under high pressure. *Rev. Mod. Phys.* **90**, 015007 (2018).
2. Mao, H.-K. High-pressure physics: sustained static generation of 1.36 to 1.72 megabars. *Science* **200**, 1145–1147 (1978).
3. Mao, H.-K. & Bell, P. M. High-pressure physics: the 1-megabar mark on the ruby R_1 static pressure scale. *Science* **191**, 851–852 (1976).
4. Jayaraman, A. Diamond anvil cell and high-pressure physical investigations. *Rev. Mod. Phys.* **55**, 65–108 (1983).
5. Wang, L. et al. Nanoprobe measurements of materials at megabar pressures. *Proc. Natl Acad. Sci. USA* **107**, 6140–6145 (2010).
6. Dubrovinsky, L., Dubrovinskaia, N., Prakapenka, V. B. & Abakumov, A. M. Implementation of micro-ball nanodiamond anvils for high-pressure studies above 6 Mbar. *Nat. Commun.* **3**, 1163 (2012).
7. Irifune, T., Kunimoto, T., Shinmei, T. & Tange, Y. High pressure generation in Kawai-type multianvil apparatus using nano-polycrystalline diamond anvils. *C. R. Geosci.* **351**, 260–268 (2019).
8. Liebermann, R. C. Multi-anvil, high pressure apparatus: a half-century of development and progress. *High Press. Res.* **31**, 493–532 (2011).
9. Dubrovinsky, L. et al. The most incompressible metal osmium at static pressures above 750 gigapascals. *Nature* **525**, 226–229 (2015).
10. Barker Jr, R. & Chen, R. Grüneisen parameter from thermal conductivity measurements under pressure. *J. Chem. Phys.* **53**, 2616–2620 (1970).
11. Walker, I. Nonmagnetic piston–cylinder pressure cell for use at 35 kbar and above. *Rev. Sci. Instrum.* **70**, 3402–3412 (1999).
12. Dubrovinskaia, N. et al. Terapascal static pressure generation with ultrahigh yield strength nanodiamond. *Sci. Adv.* **2**, e1600341 (2016).
13. Mao, H.-K., Xu, J. & Bell, P. M. Calibration of the ruby pressure gauge to 800 kbar under quasi-hydrostatic conditions. *J. Geophys. Res.* **91**, 4673–4676 (1986).
14. Akahama, Y. & Kawamura, H. Pressure calibration of diamond anvil Raman gauge to 410 GPa. *J. Phys. Conf. Ser.* **215**, 012195 (2010).
15. Chi, Z.-H. et al. Pressure-induced metallization of molybdenum disulfide. *Phys. Rev. Lett.* **113**, 036802 (2014).
16. Livneh, T. & Sterer, E. Resonant Raman scattering at exciton states tuned by pressure and temperature in 2*H*–MoS_2. *Phys. Rev. B* **81**, 195209 (2010).
17. Beck, P. et al. Measurement of thermal diffusivity at high pressure using a transient heating technique. *Appl. Phys. Lett.* **91**, 181914 (2007).
18. Hsieh, W.-P., Chen, B., Li, J., Keblinski, P. & Cahill, D. G. Pressure tuning of the thermal conductivity of the layered muscovite crystal. *Phys. Rev. B* **80**, 180302 (2009).
19. Ji, C. et al. Ultrahigh-pressure isostructural electronic transitions in hydrogen. *Nature* **573**, 558–562 (2019).
20. Celliers, P. M. et al. Insulator-metal transition in dense fluid deuterium. *Science* **361**, 677–682 (2018).
21. Chen, X.-J. et al. Enhancement of superconductivity by pressure-driven competition in electronic order. *Nature* **466**, 950–953 (2010).
22. Wang, Y. et al. Pressure-induced phase transformation, reversible amorphization, and anomalous visible light response in organolead bromide perovskite. *J. Am. Chem. Soc.* **137**, 11144–11149 (2015).
23. Knudson, M. D. et al. Direct observation of an abrupt insulator-to-metal transition in dense liquid deuterium. *Science* **348**, 1455–1460 (2015).
24. Eremets, M. I., Drozdov, A. P., Kong, P. & Wang, H. Semimetallic molecular hydrogen at pressure above 350 GPa. *Nat. Phys.* **15**, 1246–1249 (2019).
25. Cheng, B., Mazzola, G., Pickard, C. J. & Ceriotti, M. Evidence for supercritical behaviour of high-pressure liquid hydrogen. *Nature* **585**, 217–220 (2020).
26. Jiang, S. et al. A spectroscopic study of the insulator–metal transition in liquid hydrogen and deuterium. *Adv. Sci.* **7**, 1901668 (2020).
27. Drozdov, A., Eremets, M., Troyan, I., Ksenofontov, V. & Shylin, S. I. Conventional superconductivity at 203 kelvin at high pressures in the sulfur hydride system. *Nature* **525**, 73–76 (2015).
28. Drozdov, A. et al. Superconductivity at 250 K in lanthanum hydride under high pressures. *Nature* **569**, 528–531 (2019).
29. Somayazulu, M. et al. Evidence for superconductivity above 260 K in lanthanum superhydride at megabar pressures. *Phys. Rev. Lett.* **122**, 027001 (2019).
30. Snider, E. et al. Room-temperature superconductivity in a carbonaceous sulfur hydride. *Nature* **586**, 373–377 (2020).
31. Medvedev, S. et al. Electronic and magnetic phase diagram of β-$Fe_{1.01}Se$ with superconductivity at 36.7 K under pressure. *Nat. Mater.* **8**, 630–633 (2009).
32. Sun, L. et al. Re-emerging superconductivity at 48 kelvin in iron chalcogenides. *Nature* **483**, 67–69 (2012).
33. Zhao, X.-M. et al. Pressure tuning of the charge density wave and superconductivity in 2*H*–TaS_2. *Phys. Rev. B* **101**, 134506 (2020).
34. Ci, P. et al. Quantifying van der Waals interactions in layered transition metal dichalcogenides from pressure-enhanced valence band splitting. *Nano Lett.* **17**, 4982–4988 (2017).
35. Meng, X. et al. Thermal conductivity enhancement in MoS_2 under extreme strain. *Phys. Rev. Lett.* **122**, 155901 (2019).
36. Howie, R. T., Magdău, I. B., Goncharov, A. F., Ackland, G. J. & Gregoryanz, E. Phonon localization by mass disorder in dense hydrogen-deuterium binary alloy. *Phys. Rev. Lett.* **113**, 175501 (2014).
37. Howie, R. T., Dalladay-Simpson, P. & Gregoryanz, E. Raman spectroscopy of hot hydrogen above 200 GPa. *Nat. Mater.* **14**, 495–499 (2015).
38. Dalladay-Simpson, P., Howie, R. T. & Gregoryanz, E. Evidence for a new phase of dense hydrogen above 325 gigapascals. *Nature* **529**, 63–67 (2016).
39. Li, F. et al. Brillouin scattering spectroscopy for a laser heated diamond anvil cell. *Appl. Phys. Lett.* **88**, 203507 (2006).
40. Nayak, A. P. et al. Pressure-induced semiconducting to metallic transition in multilayered molybdenum disulphide. *Nat. Commun.* **5**, 3731 (2014).
41. Chi, Z.-H. et al. Superconductivity in pristine 2H_a–MoS_2 at ultrahigh pressure. *Phys. Rev. Lett.* **120**, 037002 (2018).
42. Mao, W. L. et al. Bonding changes in compressed superhard graphite. *Science* **302**, 425–427 (2003).
43. Li, Q. et al. Superhard monoclinic polymorph of carbon. *Phys. Rev. Lett.* **102**, 175506 (2009).

44. Tian, Y. et al. Ultrahard nanotwinned cubic boron nitride. *Nature* **493**, 385–388 (2013).
45. Huang, Q. et al. Nanotwinned diamond with unprecedented hardness and stability. *Nature* **510**, 250–253 (2014).
46. Ohta, K. et al. The electrical conductivity of post-perovskite in Earth's D″ layer. *Science* **320**, 89–91 (2008).
47. Konôpková, Z., McWilliams, R. S., Gómez-Pérez, N. & Goncharov, A. F. Direct measurement of thermal conductivity in solid iron at planetary core conditions. *Nature* **534**, 99–101 (2016).
48. Hsieh, W.-P. et al. Low thermal conductivity of iron-silicon alloys at Earth's core conditions with implications for the geodynamo. *Nat. Commun.* **11**, 3332 (2020).
49. Chen, X.-J. et al. Pressure-induced phonon frequency shifts in transition-metal nitrides. *Phys. Rev. B* **70**, 014501 (2004).
50. Conley, H. J. et al. Bandgap engineering of strained monolayer and bilayer MoS_2. *Nano Lett.* **13**, 3626–3630 (2013).
51. Ma, Z. et al. Pressure-induced emission of cesium lead halide perovskite nanocrystals. *Nat. Commun.* **9**, 4506 (2018).
52. Li, M., Liu, T., Wang, Y., Yang, W. & Lü, X. Pressure responses of halide perovskites with various compositions, dimensionalities, and morphologies. *Matter Radiat. Extremes* **5**, 018201 (2020).
53. Cahill, D. G. et al. Nanoscale thermal transport. *J. Appl. Phys.* **93**, 793–818 (2003).
54. Cahill, D. G. et al. Nanoscale thermal transport. II. 2003–2012. *Appl. Phys. Rev.* **1**, 011305 (2014).
55. Giri, A. & Hopkins, P. E. A review of experimental and computational advances in thermal boundary conductance and nanoscale thermal transport across solid interfaces. *Adv. Funct. Mater.* **30**, 1903857 (2020).
56. Snyder, G. J. & Toberer, E. S. Complex thermoelectric materials. *Nat. Mater.* **7**, 105–114 (2008).
57. Huxtable, S. T., Cahill, D. G. & Phinney, L. M. Thermal contact conductance of adhered microcantilevers. *J. Appl. Phys.* **95**, 2102–2108 (2004).
58. Kaviany, M. *Heat Transfer Physics* (Cambridge Univ. Press, 2014).
59. Chen, S. et al. Thermal conductivity of isotopically modified graphene. *Nat. Mater.* **11**, 203–207 (2012).
60. Li, X., Maute, K., Dunn, M. L. & Yang, R. Strain effects on the thermal conductivity of nanostructures. *Phys. Rev. B* **81**, 245318 (2010).
61. Ding, Z., Pei, Q.-X., Jiang, J.-W. & Zhang, Y.-W. Manipulating the thermal conductivity of monolayer MoS_2 via lattice defect and strain engineering. *J. Phys. Chem. C* **119**, 16358–16365 (2015).
62. Wei, Z., Chen, Y. & Dames, C. Negative correlation between in-plane bonding strength and cross-plane thermal conductivity in a model layered material. *Appl. Phys. Lett.* **102**, 011901 (2013).
63. Lindsay, L., Broido, D. A., Carrete, J., Mingo, N. & Reinecke, T. L. Anomalous pressure dependence of thermal conductivities of large mass ratio compounds. *Phys. Rev. B* **91**, 121202 (2015).
64. Ouyang, T. & Hu, M. Competing mechanism driving diverse pressure dependence of thermal conductivity of *X*Te (*X*=Hg, Cd, and Zn). *Phys. Rev. B* **92**, 235204 (2015).
65. Ravichandran, N. K. & Broido, D. Non-monotonic pressure dependence of the thermal conductivity of boron arsenide. *Nat. Commun.* **10**, 827 (2019).
66. Chen, L.-C. et al. Enhancement of thermoelectric performance across the topological phase transition in dense lead selenide. *Nat. Mater.* **18**, 1321–1326 (2019).
67. Ross, R. G., Andersson, P., Sundqvist, B. & Backstrom, G. Thermal conductivity of solids and liquids under pressure. *Rep. Prog. Phys.* **47**, 1347–1402 (1984).
68. Hofmeister, A. M. Pressure dependence of thermal transport properties. *Proc. Natl Acad. Sci. USA* **104**, 9192–9197 (2007).
69. Chen, J., Walther, J. H. & Koumoutsakos, P. Strain engineering of Kapitza resistance in few-layer graphene. *Nano Lett.* **14**, 819–825 (2014).
70. Hohensee, G. T., Wilson, R. & Cahill, D. G. Thermal conductance of metal–diamond interfaces at high pressure. *Nat. Commun.* **6**, 6578 (2015).
71. Vandersande, J. & Wood, C. The thermal conductivity of insulators and semiconductors. *Contemp. Phys.* **27**, 117–144 (1986).
72. Wang, Y., Qiu, B., J. H. McGaughey, A., Ruan, X. & Xu, X. Mode-wise thermal conductivity of bismuth telluride. *J. Heat Transf.* **135**, 091102 (2013).
73. Borca-Tasciuc, D.-A. et al. Thermal properties of electrodeposited bismuth telluride nanowires embedded in amorphous alumina. *Appl. Phys. Lett.* **85**, 6001–6003 (2004).
74. Mavrokefalos, A. et al. Thermoelectric and structural characterizations of individual electrodeposited bismuth telluride nanowires. *J. Appl. Phys.* **105**, 104318 (2009).
75. Park, K. H., Mohamed, M., Aksamija, Z. & Ravaioli, U. Phonon scattering due to van der Waals forces in the lattice thermal conductivity of Bi_2Te_3 thin films. *J. Appl. Phys.* **117**, 015103 (2015).
76. Al-Alam, P. et al. Lattice thermal conductivity of Bi_2Te_3 and SnSe using Debye-Callaway and Monte Carlo phonon transport modeling: application to nanofilms and nanowires. *Phys. Rev. B* **100**, 115304 (2019).
77. Prasher, R. Acoustic mismatch model for thermal contact resistance of van der Waals contacts. *Appl. Phys. Lett.* **94**, 041905 (2009).
78. Huang, B.-L. & Kaviany, M. Ab initio and molecular dynamics predictions for electron and phonon transport in bismuth telluride. *Phys. Rev. B* **77**, 125209 (2008).
79. Qiu, B. & Ruan, X. Molecular dynamics simulations of lattice thermal conductivity of bismuth telluride using two-body interatomic potentials. *Phys. Rev. B* **80**, 165203 (2009).
80. Termentzidis, K. et al. Large thermal conductivity decrease in point defective Bi_2Te_3 bulk materials and superlattices. *J. Appl. Phys.* **113**, 013506 (2013).
81. Kapitza, P. L. Heat transfer and superfluidity of helium II. *Phys. Rev.* **60**, 354–355 (1941).
82. Pop, E. Energy dissipation and transport in nanoscale devices. *Nano Res.* **3**, 147–169 (2010).
83. Kuball, M. & Pomeroy, J. W. A review of Raman thermography for electronic and opto-electronic device measurement with submicron spatial and nanosecond temporal resolution. *IEEE Trans. Device Mater. Reliab.* **16**, 667–684 (2016).
84. Siegrist, T., Merkelbach, P. & Wuttig, M. Phase change materials: challenges on the path to a universal storage device. *Annu. Rev. Condens. Matter Phys.* **3**, 215–237 (2012).
85. Wuttig, M., Bhaskaran, H. & Taubner, T. Phase-change materials for non-volatile photonic applications. *Nat. Photonics* **11**, 465–476 (2017).
86. Costescu, R. M., Cahill, D. G., Fabreguette, F. H., Sechrist, Z. A. & George, S. M. Ultra-low thermal conductivity in W/Al_2O_3 nanolaminates. *Science* **303**, 989–990 (2004).
87. Losego, M. D., Blitz, I. P., Vaia, R. A., Cahill, D. G. & Braun, P. V. Ultralow thermal conductivity in organoclay nanolaminates synthesized via simple self-assembly. *Nano Lett.* **13**, 2215–2219 (2013).
88. Giri, A., Donovan, B. F. & Hopkins, P. E. Localization of vibrational modes leads to reduced thermal conductivity of amorphous heterostructures. *Phys. Rev. Mater.* **2**, 056002 (2018).
89. Merabia, S., Shenogin, S., Joly, L., Keblinski, P. & Barrat, J.-L. Heat transfer from nanoparticles: a corresponding state analysis. *Proc. Natl Acad. Sci. USA* **106**, 15113–15118 (2009).
90. Little, W. The transport of heat between dissimilar solids at low temperatures. *Can. J. Phys.* **37**, 334–349 (1959).
91. Swartz, E. & Pohl, R. Thermal resistance at interfaces. *Appl. Phys. Lett.* **51**, 2200–2202 (1987).
92. Swartz, E. T. & Pohl, R. O. Thermal boundary resistance. *Rev. Mod. Phys.* **61**, 605–668 (1989).
93. Stoner, R. & Maris, H. Kapitza conductance and heat flow between solids at temperatures from 50 to 300 K. *Phys. Rev. B* **48**, 16373 (1993).
94. Stevens, R. J., Smith, A. N. & Norris, P. M. Measurement of thermal boundary conductance of a series of metal-dielectric interfaces by the transient thermoreflectance technique. *J. Heat Transf.* **127**, 315–322 (2005).
95. Snyder, N. Heat transport through helium II: Kapitza conductance. *Cryogenics* **10**, 89–95 (1970).
96. Lyeo, H.-K. & Cahill, D. G. Thermal conductance of interfaces between highly dissimilar materials. *Phys. Rev. B* **73**, 144301 (2006).
97. Hopkins, P. E., Norris, P. M. & Stevens, R. J. Influence of inelastic scattering at metal-dielectric interfaces. *J. Heat Transf.* **130**, 022401 (2008).
98. Stevens, R. J., Zhigilei, L. V. & Norris, P. M. Effects of temperature and disorder on thermal boundary conductance at solid–solid interfaces: nonequilibrium molecular dynamics simulations. *Int. J. Heat Mass Transf.* **50**, 3977–3989 (2007).
99. Zha, C.-S., Mao, H.-K. & Hemley, R. J. Elasticity of MgO and a primary pressure scale to 55 GPa. *Proc. Natl Acad. Sci. USA* **97**, 13494–13499 (2000).
100. Spetzler, H. et al. Ultrasonic measurements in a diamond anvil cell. *Phys. Earth Planet. Inter.* **98**, 93–99 (1996).
101. Jacobsen, S. D. et al. Structure and elasticity of single-crystal (Mg,Fe)O and a new method of generating shear waves for gigahertz ultrasonic interferometry. *J. Geophys. Res Solid Earth* **107**, ECV 4-1–ECV 4-14 (2002).
102. Jacobsen, S. D., Spetzler, H., Reichmann, H. J. & Smyth, J. R. Shear waves in the diamond-anvil cell reveal pressure-induced instability in (Mg,Fe)O. *Proc. Natl Acad. Sci. USA* **101**, 5867–5871 (2004).
103. Decremps, F. et al. Sound velocity of iron up to 152 GPa by picosecond acoustics in diamond anvil cell. *Geophys. Res. Lett.* **41**, 1459–1464 (2014).
104. Mao, H.-K. et al. Phonon density of states of iron up to 153 gigapascals. *Science* **292**, 914–916 (2001).
105. Farber, D. L. et al. Lattice dynamics of molybdenum at high pressure. *Phys. Rev. Lett.* **96**, 115502 (2006).
106. Loa, I. et al. Lattice dynamics and superconductivity in cerium at high pressure. *Phys. Rev. Lett.* **108**, 045502 (2012).
107. Klotz, S. et al. Phonon dispersion measurements at high pressures to 7 GPa by inelastic neutron scattering. *Appl. Phys. Lett.* **66**, 1557–1559 (1995).
108. Klotz, S. et al. Pressure induced frequency shifts of transverse acoustic phonons in germanium to 9.7 GPa. *Phys. Rev. Lett.* **79**, 1313–1316 (1997).
109. Klotz, S. Phonon dispersion curves by inelastic neutron scattering to 12 GPa. *Z. Kristallogr. Cryst. Mater.* **216**, 420–429 (2001).
110. Sun, Z., Yuan, K., Zhang, X. & Tang, D. Pressure tuning of the thermal conductivity of gallium arsenide from first-principles calculations. *Phys. Chem. Chem. Phys.* **20**, 30331–30339 (2018).
111. Yu, H. et al. Large enhancement of thermoelectric performance in $CuInTe_2$ upon compression. *Mater. Today Phys.* **5**, 1–6 (2018).
112. Wang, L. et al. High-pressure phases of boron arsenide with potential high thermal conductivity. *Phys. Rev. B* **99**, 174104 (2019).
113. Saha, P., Mazumder, A. & Mukherjee, G. D. Thermal conductivity of dense hcp iron: direct measurements using laser heated diamond anvil cell. *Geosci. Front.* **11**, 1755–1761 (2020).
114. Yuan, K., Zhang, X., Tang, D. & Hu, M. Anomalous pressure effect on the thermal conductivity of ZnO, GaN, and AlN from first-principles calculations. *Phys. Rev. B* **98**, 144303 (2018).
115. Lan, G., Ouyang, B. & Song, J. The role of low-lying optical phonons in lattice thermal conductance of rare-earth pyrochlores: a first-principle study. *Acta Mater.* **91**, 304–317 (2015).
116. Zhao, D., Qian, X., Gu, X., Jajja, S. A. & Yang, R. Measurement techniques for thermal conductivity and interfacial thermal conductance of bulk and thin film materials. *J. Electron. Packag.* **138**, 040802 (2016).
117. Tritt, T. M. & Weston, D. in *Thermal Conductivity: Theory, Properties, and Applications* (ed. Tritt, T. M.) 187–203 (Springer, 2004).
118. Pope, A. L., Zawilski, B. & Tritt, T. M. Description of removable sample mount apparatus for rapid thermal conductivity measurements. *Cryogenics* **41**, 725–731 (2001).
119. Zawilski, B. M., Littleton IV, R. T. & Tritt, T. M. Description of the parallel thermal conductance technique for the measurement of the thermal conductivity of small diameter samples. *Rev. Sci. Instrum.* **72**, 1770–1774 (2001).
120. Völklein, F. Thermal conductivity and diffusivity of a thin film SiO_2–Si_3N_4 sandwich system. *Thin Solid Films* **188**, 27–33 (1990).
121. Völklein, F., Reith, H. & Meier, A. Measuring methods for the investigation of in-plane and cross-plane thermal conductivity of thin films. *Phys. Status Solidi A* **210**, 106–118 (2013).
122. Borca-Tasciuc, T. & Chen, G. in *Thermal Conductivity: Theory, Properties, and Applications* (ed. Tritt, T. M.) 205–237 (Springer, 2004).
123. Balandin, A. A. et al. Superior thermal conductivity of single-layer graphene. *Nano Lett.* **8**, 902–907 (2008).
124. Maldonado, O. Pulse method for simultaneous measurement of electric thermopower and heat conductivity at low temperatures. *Cryogenics* **32**, 908–912 (1992).
125. Stalhane, B. & Pyk, S. New method for determining the coefficients of thermal conductivity. *Tek. Tidskr.* **61**, 389–393 (1931).
126. Gustafsson, S. E. Transient plane source techniques for thermal conductivity and thermal diffusivity

measurements of solid materials. *Rev. Sci. Instrum.* **62**, 797–804 (1991).
127. Cahill, D. G. Thermal conductivity measurement from 30 to 750 K: the 3ω method. *Rev. Sci. Instrum.* **61**, 802–808 (1990).
128. Parker, W. J., Jenkins, R. J., Butler, C. P. & Abbott, G. L. Flash method of determining thermal diffusivity, heat capacity, and thermal conductivity. *J. Appl. Phys.* **32**, 1679–1684 (1961).
129. Rosencwaig, A. & Gersho, A. Theory of the photoacoustic effect with solids. *J. Appl. Phys.* **47**, 64–69 (1976).
130. Cahill, D. G. Analysis of heat flow in layered structures for time-domain thermoreflectance. *Rev. Sci. Instrum.* **75**, 5119–5122 (2004).
131. Schmidt, A. J., Cheaito, R. & Chiesa, M. A frequency-domain thermoreflectance method for the characterization of thermal properties. *Rev. Sci. Instrum.* **80**, 094901 (2009).
132. Fujisawa, H., Fujii, N., Mizutani, H., Kanamori, H. & Akimoto, S. I. Thermal diffusivity of Mg_2SiO_4, Fe_2SiO_4, and NaCl at high pressures and temperatures. *J. Geophys. Res.* **73**, 4727–4733 (1968).
133. Håkansson, B., Andersson, P. & Bäckström, G. Improved hot-wire procedure for thermophysical measurements under pressure. *Rev. Sci. Instrum.* **59**, 2269–2275 (1988).
134. Katsura, T. Thermal diffusivity of silica glass at pressures up to 9 GPa. *Phys. Chem. Miner.* **20**, 201–208 (1993).
135. Xu, Y. et al. Thermal diffusivity and conductivity of olivine, wadsleyite and ringwoodite to 20 GPa and 1373 K. *Phys. Earth Planet. Inter.* **143–144**, 321–336 (2004).
136. Bercegeay, C. & Bernard, S. First-principles equations of state and elastic properties of seven metals. *Phys. Rev. B* **72**, 214101 (2005).
137. Hsieh, W.-P. et al. Testing the minimum thermal conductivity model for amorphous polymers using high pressure. *Phys. Rev. B* **83**, 174205 (2011).
138. Park, C. H., Cheong, B. H., Lee, K. H. & Chang, K. J. Structural and electronic properties of cubic, 2*H*, 4*H*, and 6*H* SiC. *Phys. Rev. B* **49**, 4485–4493 (1994).
139. Xie, J., Chen, S.-P., Tse, J. S., de Gironcoli, S. & Baroni, S. High-pressure thermal expansion, bulk modulus, and phonon structure of diamond. *Phys. Rev. B* **60**, 9444–9449 (1999).
140. Manthilake, M. A. G. M., de Koker, N. & Frost, D. J. Thermal conductivity of $CaGeO_3$ perovskite at high pressure. *Geophys. Res. Lett.* **38**, L08301 (2011).
141. Barker, R. Jr, Chen, R. & Frost, R. Influence of pressure and chemical structure on the thermal conductivity of vitreous poly(alkyl methacrylates). I. *J. Polym. Sci. Polym. Phys.* **15**, 1199–1210 (1977).
142. Frost, R. S., Chen, R. Y. S. & Barker, R. E. Pressure dependence of thermal conductivity in polyethylene. *J. Appl. Phys.* **46**, 4506–4509 (1975).
143. Hsieh, W.-P. *Testing Theories for Thermal Transport Using High Pressure*. Thesis, Univ. Illinois at Urbana-Champaign (2012).
144. Katsura, T. Thermal diffusivity of olivine under upper mantle conditions. *Geophys. J. Int.* **122**, 63–69 (1995).
145. Frost, D. J. et al. A new large-volume multianvil system. *Phys. Earth Planet. Inter.* **143–144**, 507–514 (2004).
146. Manthilake, G. M., de Koker, N., Frost, D. J. & McCammon, C. A. Lattice thermal conductivity of lower mantle minerals and heat flux from Earth's core. *Proc. Natl Acad. Sci. USA* **108**, 17901 (2011).
147. Abramson, E. H., Brown, J. M. & Slutsky, L. J. The thermal diffusivity of water at high pressures and temperatures. *J. Chem. Phys.* **115**, 10461–10463 (2001).
148. Abramson, E. H., Slutsky, L. J. & Brown, J. M. Thermal diffusivity of fluid oxygen to 12 GPa and 300 °C. *J. Chem. Phys.* **111**, 9357–9360 (1999).
149. Chai, M., Brown, J. M. & Slutsky, L. J. Thermal diffusivity of mantle minerals. *Phys. Chem. Miner.* **23**, 470–475 (1996).
150. Yue, D. et al. Accurate temperature measurement by temperature field analysis in diamond anvil cell for thermal transport study of matter under high pressures. *Appl. Phys. Lett.* **112**, 081901 (2018).
151. Pang, H.-J. et al. Pressure tuning of thermoelectric performance in FeNbSb. *J. Alloys Compd.* **805**, 1224–1230 (2019).
152. Chen, L.-C. et al. Pressure-induced enhancement of thermoelectric performance in palladium sulfide. *Mater. Today Phys.* **5**, 64–71 (2018).
153. Håkansson, B. & Ross, R. G. Effective thermal conductivity of binary dispersed composites over wide ranges of volume fraction, temperature, and pressure. *J. Appl. Phys.* **68**, 3285–3292 (1990).
154. Andersson, O. & Suga, H. Thermal conductivity of the *Ih* and XI phases of ice. *Phys. Rev. B* **50**, 6583–6588 (1994).
155. Andersson, O. & Suga, H. Thermal conductivity of normal and deuterated tetrahydrofuran clathrate hydrates. *J. Phys. Chem. Solids* **57**, 125–132 (1996).
156. Andersson, O., Soldatov, A. & Sundqvist, B. Thermal conductivity of C_{60} at pressures up to 1 GPa and temperatures in the 50–300 K range. *Phys. Rev. B* **54**, 3093–3100 (1996).
157. Larsson, R. & Andersson, O. Lubricant thermal conductivity and heat capacity under high pressure. *Proc. Inst. Mech. Eng. J. J. Eng. Tribol.* **214**, 337–342 (2000).
158. Andersson, O., Chobal, O., Rizak, I., Rizak, V. & Sabadosh, V. Effects of pressure and temperature on the thermal conductivity of $Sn_2P_2S_6$. *Phys. Rev. B* **83**, 134121 (2011).
159. Yu, J., Tonpheng, B., Gröbner, G. & Andersson, O. Thermal properties and transition studies of multi-wall carbon nanotube/nylon-6 composites. *Carbon* **49**, 4858–4866 (2011).
160. Andersson, O. Thermal conductivity of normal and deuterated water, crystalline ice, and amorphous ices. *J. Chem. Phys.* **149**, 124506 (2018).
161. Soldatov, A. & Sundqvist, B. Molecular rotation in C_{70} at high pressures: a thermal conductivity study. *J. Phys. Chem. Solids* **57**, 1371–1375 (1996).
162. Franco, A. An apparatus for the routine measurement of thermal conductivity of materials for building application based on a transient hot-wire method. *Appl. Therm. Eng.* **27**, 2495–2504 (2007).
163. Osako, M., Ito, E. & Yoneda, A. Simultaneous measurements of thermal conductivity and thermal diffusivity for garnet and olivine under high pressure. *Phys. Earth Planet. Inter.* **143-144**, 311–320 (2004).
164. Yoneda, A., Osako, M. & Ito, E. Heat capacity measurement under high pressure: a finite element method assessment. *Phys. Earth Planet. Inter.* **174**, 309–314 (2009).
165. Goncharov, A. F., Beck, P., Struzhkin, V. V., Haugen, B. D. & Jacobsen, S. D. Thermal conductivity of lower-mantle minerals. *Phys. Earth Planet. Inter.* **174**, 24–32 (2009).
166. Goncharov, A. F. et al. Effect of composition, structure, and spin state on the thermal conductivity of the Earth's lower mantle. *Phys. Earth Planet. Inter.* **180**, 148–153 (2010).
167. Chiritescu, C. et al. Ultralow thermal conductivity in disordered, layered WSe_2 crystals. *Science* **315**, 351–353 (2007).
168. Ge, Z., Cahill, D. G. & Braun, P. V. Thermal conductance of hydrophilic and hydrophobic interfaces. *Phys. Rev. Lett.* **96**, 186101 (2006).
169. Beran, A. The reflectance behaviour of gold at temperatures up to 500 °C. *Tschermaks Min. Petr. Mitt.* **34**, 211–215 (1985).
170. Hsieh, W.-P. & Cahill, D. G. Ta and Au(Pd) alloy metal film transducers for time-domain thermoreflectance at high pressures. *J. Appl. Phys.* **109**, 113520 (2011).
171. Hsieh, W.-P. Thermal conductivity of methanol-ethanol mixture and silicone oil at high pressures. *J. Appl. Phys.* **117**, 235901 (2015).
172. Jeong, J. et al. Picosecond transient thermoreflectance for thermal conductivity characterization. *Nanoscale Microscale Thermophys. Eng.* **23**, 211–221 (2019).
173. Hasegawa, A., Yagi, T. & Ohta, K. Combination of pulsed light heating thermoreflectance and laser-heated diamond anvil cell for in-situ high pressure-temperature thermal diffusivity measurements. *Rev. Sci. Instrum.* **90**, 074901 (2019).
174. McWilliams, R. S., Konôpková, Z. & Goncharov, A. F. A flash heating method for measuring thermal conductivity at high pressure and temperature: application to Pt. *Phys. Earth Planet. Inter.* **247**, 17–26 (2015).
175. Geballe, Z. M., Sime, N., Badro, J., van Keken, P. E. & Goncharov, A. F. Thermal conductivity near the bottom of the Earth's lower mantle: measurements of pyrolite up to 120 GPa and 2500 K. *Earth Planet. Sci. Lett.* **536**, 116161 (2020).
176. Hsieh, W.-P., Lyons, A. S., Pop, E., Keblinski, P. & Cahill, D. G. Pressure tuning of the thermal conductance of weak interfaces. *Phys. Rev. B* **84**, 184107 (2011).
177. Okuda, Y. et al. Thermal conductivity of Fe-bearing post-perovskite in the Earth's lowermost mantle. *Earth Planet Sci. Lett.* **547**, 116466 (2020).
178. Hamrin, C. E. & Thodos, G. The thermal conductivity of hydrogen for pressures up to 660atm and temperatures between 1.6 and 74.6 °C. *Physica* **32**, 918–932 (1966).
179. Roder, H. M. The thermal conductivity of oxygen. *J. Res. Natl Bur. Stand.* **87**, 279–310 (1982).
180. Roder, H. M. Thermal conductivity of methane for temperatures between 110 and 310 K with pressures to 70 MPa. *Int. J. Thermophys.* **6**, 119–142 (1985).
181. Gilmore, T. F. & Comings, E. W. Thermal conductivity of binary mixtures of carbon dioxide, nitrogen, and ethane at high pressures: comparison with correlation and theory. *AIChE J.* **12**, 1172–1178 (1966).
182. Sengers, J. V., Bolk, W. T. & Stigter, C. J. The thermal conductivity of neon between 25 °C and 75 °C at pressures up to 2600 atmospheres. *Physica* **30**, 1018–1026 (1964).
183. Millat, J., Mustafa, M., Ross, M., Wakeham, W. A. & Zalaf, M. The thermal conductivity of argon, carbon dioxide and nitrous oxide. *Phys. A Stat. Mech. Appl.* **145**, 461–497 (1987).
184. Goncharov, A. F. et al. Thermal conductivity of argon at high pressures and high temperatures. *J. Appl. Phys.* **111**, 112609 (2012).
185. Tretiakov, K. V. & Scandolo, S. Thermal conductivity of solid argon at high pressure and high temperature: a molecular dynamics study. *J. Chem. Phys.* **121**, 11177–11182 (2004).
186. Chernatynskiy, A. & Phillpot, S. R. Thermal conductivity of argon at high pressure from first principles calculations. *J. Appl. Phys.* **114**, 064902 (2013).
187. Zaghoo, M. & Silvera, I. F. Conductivity and dissociation in liquid metallic hydrogen and implications for planetary interiors. *Proc. Natl Acad. Sci. USA* **114**, 11873–11877 (2017).
188. Ramaswamy, R., Balasubramaniam, V. M. & Sastry, S. K. Thermal conductivity of selected liquid foods at elevated pressures up to 700 MPa. *J. Food Eng.* **83**, 444–451 (2007).
189. Shulga, V. M., Eldarov, F. G., Atanov, Y. A. & Kuyumchev, A. A. Thermal conductivity and heat capacity of liquid toluene at temperatures between 255 and 400 K and at pressures up to 1000 MPa. *Int. J. Thermophys.* **7**, 1147–1161 (1986).
190. Yebra, F., Troncoso, J. & Romaní, L. Thermal conductivity measurements for organic liquids at high pressure. *J. Chem. Thermodyn.* **142**, 106005 (2020).
191. Chen, B., Hsieh, W.-P., Cahill, D. G., Trinkle, D. R. & Li, J. Thermal conductivity of compressed H_2O to 22 GPa: a test of the Leibfried-Schlomann equation. *Phys. Rev. B* **83**, 132301 (2011).
192. Ross, R. G. & Sandberg, O. The thermal conductivity of four solid phases of NH_4F, and a comparison with H_2O. *J. Phys. C Solid State Phys.* **11**, 667–672 (1978).
193. Jacobsen, M. K., Sinogeikin, S. V., Kumar, R. S. & Cornelius, A. L. High pressure transport characteristics of Bi_2Te_3, Sb_2Te_3, and $BiSbTe_3$. *J. Phys. Chem. Solids* **73**, 1154–1158 (2012).
194. Yu, C., Zhang, G., Zhang, Y.-W. & Peng, L.-M. Strain engineering on the thermal conductivity and heat flux of thermoelectric Bi_2Te_3 nanofilm. *Nano Energy* **17**, 104–110 (2015).
195. Jacobsen, M. K., Kumar, R. S. & Cornelius, A. L. Transport properties of Ni and PbTe under pressure. *J. Electron. Mater.* **41**, 633–638 (2012).
196. Morozova, N. V., Korobeinikov, I. V. & Ovsyannikov, S. V. Strategies and challenges of high-pressure methods applied to thermoelectric materials. *J. Appl. Phys.* **125**, 220901 (2019).
197. Ovsyannikov, S. V. & Shchennikov, V. V. Pressure-tuned colossal improvement of thermoelectric efficiency of PbTe. *Appl. Phys. Lett.* **90**, 122103 (2007).
198. Yang, X. et al. Pressure induced excellent thermoelectric behavior in skutterudites $CoSb_3$ and $IrSb_3$. *Phys. Chem. Chem. Phys.* **21**, 851–858 (2019).
199. Boehler, R. & Ramakrishnan, J. Experimental results on the pressure dependence of the Grüneisen parameter: a review. *J. Geophys. Res. Solid Earth* **85**, 6996–7002 (1980).
200. Boehler, R. Adiabats $(\partial T/\partial P)_s$ and Grüneisen parameter of NaCl up to 50 kilobars and 800 °C. *J. Geophys. Res. Solid Earth* **86**, 7159–7162 (1981).
201. Anderson, O. L. The Grüneisen ratio for the last 30 years. *Geophys. J. Int.* **143**, 279–294 (2000).
202. Hofmeister, A. M. & Mao, H.-K. Redefinition of the mode Grüneisen parameter for polyatomic substances and thermodynamic implications. *Proc. Natl Acad. Sci. USA* **99**, 559–564 (2002).
203. Dorogokupets, P. I. & Dewaele, A. Equations of state of MgO, Au, Pt, NaCl-B1, and NaCl-B2: internally consistent high-temperature pressure scales. *High Press. Res.* **27**, 431–446 (2007).

204. Dewaele, A., Datchi, F., Loubeyre, P. & Mezouar, M. High pressure–high temperature equations of state of neon and diamond. *Phys. Rev. B* **77**, 094106 (2008).
205. Pozzo, M., Davies, C., Gubbins, D. & Alfè, D. Thermal and electrical conductivity of iron at Earth's core conditions. *Nature* **485**, 355–358 (2012).
206. McWilliams, R. S., Dalton, D. A., Konōpková, Z., Mahmood, M. F. & Goncharov, A. F. Opacity and conductivity measurements in noble gases at conditions of planetary and stellar interiors. *Proc. Natl Acad. Sci. USA* **112**, 7925–7930 (2015).
207. Basu, A., Field, M. R., McCulloch, D. G. & Boehler, R. New measurement of melting and thermal conductivity of iron close to outer core conditions. *Geosci. Front.* **11**, 565–568 (2020).
208. Xu, J. et al. Thermal conductivity and electrical resistivity of solid iron at Earth's core conditions from first principles. *Phys. Rev. Lett.* **121**, 096601 (2018).
209. de Koker, N., Steinle-Neumann, G. & Vlček, V. Electrical resistivity and thermal conductivity of liquid Fe alloys at high P and T, and heat flux in Earth's core. *Proc. Natl Acad. Sci. USA* **109**, 4070–4073 (2012).
210. Ohta, K., Kuwayama, Y., Hirose, K., Shimizu, K. & Ohishi, Y. Experimental determination of the electrical resistivity of iron at Earth's core conditions. *Nature* **534**, 95–98 (2016).
211. Seagle, C. T., Cottrell, E., Fei, Y., Hummer, D. R. & Prakapenka, V. B. Electrical and thermal transport properties of iron and iron-silicon alloy at high pressure. *Geophys. Res. Lett.* **40**, 5377–5381 (2013).
212. Tang, X. & Dong, J. Lattice thermal conductivity of MgO at conditions of Earth's interior. *Proc. Natl Acad. Sci. USA* **107**, 4539–4543 (2010).
213. Tang, X. & Dong, J. Pressure dependence of harmonic and anharmonic lattice dynamics in MgO: a first-principles calculation and implications for lattice thermal conductivity. *Phys. Earth Planet. Inter.* **174**, 33–38 (2009).
214. Goncharov, A. F., Haugen, B. D., Struzhkin, V. V., Beck, P. & Jacobsen, S. D. Radiative conductivity in the Earth's lower mantle. *Nature* **456**, 231–234 (2008).
215. Goncharov, A. F., Struzhkin, V. V. & Jacobsen, S. D. Reduced radiative conductivity of low-spin (Mg,Fe)O in the lower mantle. *Science* **312**, 1205–1208 (2006).
216. Lobanov, S. S., Holtgrewe, N., Lin, J.-F. & Goncharov, A. F. Radiative conductivity and abundance of post-perovskite in the lowermost mantle. *Earth Planet. Sci. Lett.* **479**, 43–49 (2017).
217. Lobanov, S. S. et al. Blocked radiative heat transport in the hot pyrolitic lower mantle. *Earth Planet. Sci. Lett.* **537**, 116176 (2020).
218. Dalton, D. A., Hsieh, W.-P., Hohensee, G. T., Cahill, D. G. & Goncharov, A. F. Effect of mass disorder on the lattice thermal conductivity of MgO periclase under pressure. *Sci. Rep.* **3**, 2400 (2013).
219. Stackhouse, S., Stixrude, L. & Karki, B. B. Thermal conductivity of periclase (MgO) from first principles. *Phys. Rev. Lett.* **104**, 208501 (2010).
220. de Koker, N. Thermal conductivity of MgO periclase at high pressure: implications for the D″ region. *Earth Planet. Sci. Lett.* **292**, 392–398 (2010).
221. Hsieh, W.-P., Deschamps, F., Okuchi, T. & Lin, J.-F. Effects of iron on the lattice thermal conductivity of Earth's deep mantle and implications for mantle dynamics. *Proc. Natl Acad. Sci. USA* **115**, 4099–4104 (2018).
222. Hsieh, W.-P., Deschamps, F., Okuchi, T. & Lin, J.-F. Reduced lattice thermal conductivity of Fe-bearing bridgmanite in Earth's deep mantle. *J. Geophys. Res. Solid Earth* **122**, 4900–4917 (2017).
223. Chao, K.-H. & Hsieh, W.-P. Thermal conductivity anomaly in $(Fe_{0.78}Mg_{0.22})CO_3$ siderite across spin transition of iron. *J. Geophys. Res. Solid Earth* **124**, 1388–1396 (2019).
224. Hsieh, W.-P. et al. Spin transition of iron in δ-(Al,Fe)OOH induces thermal anomalies in Earth's lower mantle. *Geophys. Res. Lett.* **47**, e2020GL087036 (2020).
225. Goncharov, A. F. et al. Experimental study of thermal conductivity at high pressures: implications for the deep Earth's interior. *Phys. Earth Planet. Inter.* **247**, 11–16 (2015).
226. Yagi, T. et al. Thermal diffusivity measurement in a diamond anvil cell using a light pulse thermoreflectance technique. *Meas. Sci. Technol.* **22**, 024011 (2010).
227. Chang, Y.-Y., Hsieh, W.-P., Tan, E. & Chen, J. Hydration-reduced lattice thermal conductivity of olivine in Earth's upper mantle. *Proc. Natl Acad. Sci. USA* **114**, 4078 (2017).
228. Marzotto, E. et al. Effect of water on lattice thermal conductivity of ringwoodite and its implications for the thermal evolution of descending slabs. *Geophys. Res. Lett.* **47**, e2020GL087607 (2020).
229. Ohta, K. et al. Lattice thermal conductivity of $MgSiO_3$ perovskite and post-perovskite at the core–mantle boundary. *Earth Planet. Sci. Lett.* **349-350**, 109–115 (2012).
230. Osako, M. & Ito, E. Thermal diffusivity of $MgSiO_3$ perovskite. *Geophys. Res. Lett.* **18**, 239–242 (1991).
231. Hofmeister, A. M. Mantle values of thermal conductivity and the geotherm from phonon lifetimes. *Science* **283**, 1699–1706 (1999).
232. Hofmeister, A. M. Inference of high thermal transport in the lower mantle from laser-flash experiments and the damped harmonic oscillator model. *Phys. Earth Planet. Inter.* **170**, 201–206 (2008).
233. Okuda, Y. et al. The effect of iron and aluminum incorporation on lattice thermal conductivity of bridgmanite at the Earth's lower mantle. *Earth Planet. Sci. Lett.* **474**, 25–31 (2017).
234. Ohta, K., Yagi, T., Hirose, K. & Ohishi, Y. Thermal conductivity of ferropericlase in the Earth's lower mantle. *Earth Planet. Sci. Lett.* **465**, 29–37 (2017).
235. Haigis, V., Salanne, M. & Jahn, S. Thermal conductivity of MgO, $MgSiO_3$ perovskite and post-perovskite in the Earth's deep mantle. *Earth Planet. Sci. Lett.* **355**, 102–108 (2012).
236. Ammann, M. W. et al. Variation of thermal conductivity and heat flux at the Earth's core mantle boundary. *Earth Planet. Sci. Lett.* **390**, 175–185 (2014).
237. Tang, X., Ntam, M. C., Dong, J., Rainey, E. S. G. & Kavner, A. The thermal conductivity of Earth's lower mantle. *Geophys. Res. Lett.* **41**, 2746–2752 (2014).
238. Stackhouse, S., Stixrude, L. & Karki, B. B. First-principles calculations of the lattice thermal conductivity of the lower mantle. *Earth Planet. Sci. Lett.* **427**, 11–17 (2015).
239. Hohensee, G. T., Fellinger, M. R., Trinkle, D. R. & Cahill, D. G. Thermal transport across high-pressure semiconductor-metal transition in Si and $Si_{0.991}Ge_{0.009}$. *Phys. Rev. B* **91**, 205104 (2015).
240. Broido, D. A., Lindsay, L. & Ward, A. Thermal conductivity of diamond under extreme pressure: a first-principles study. *Phys. Rev. B* **86**, 115203 (2012).
241. Slack, G. A. & Andersson, P. Pressure and temperature effects on the thermal conductivity of CuCl. *Phys. Rev. B* **26**, 1873–1884 (1982).
242. Ulrich, C., Göbel, A., Syassen, K. & Cardona, M. Pressure-induced disappearance of the Raman anomaly in CuCl. *Phys. Rev. Lett.* **82**, 351–354 (1999).
243. Ulrich, C., Syassen, K., Cardona, M., Cros, A. & Cantarero, A. Lattice phonon modes of the high-pressure phase CuCl-IV. *Phys. Rev. B* **60**, 9410–9415 (1999).
244. Liu, J., Choi, G. M. & Cahill, D. G. Measurement of the anisotropic thermal conductivity of molybdenum disulfide by the time-resolved magneto-optic Kerr effect. *J. Appl. Phys.* **116**, 233107 (2014).
245. Jo, I., Pettes, M. T., Ou, E., Wu, W. & Shi, L. Basal-plane thermal conductivity of few-layer molybdenum disulfide. *Appl. Phys. Lett.* **104**, 201902 (2014).
246. Sahoo, S., Gaur, A. P. S., Ahmadi, M., Guinel, M. J. F. & Katiyar, R. S. Temperature-dependent Raman studies and thermal conductivity of few-layer MoS_2. *J. Phys. Chem. C* **117**, 9042–9047 (2013).
247. Muratore, C. et al. Cross-plane thermal properties of transition metal dichalcogenides. *Appl. Phys. Lett.* **102**, 081604 (2013).
248. Jiang, P., Qian, X., Gu, X. & Yang, R. Probing anisotropic thermal conductivity of transition metal dichalcogenides MX_2 (M = Mo, W and X = S, Se) using time-domain thermoreflectance. *Adv. Mater.* **29**, 1701068 (2017).
249. Wang, X. & Tabarraei, A. Phonon thermal conductivity of monolayer MoS_2. *Appl. Phys. Lett.* **108**, 191905 (2016).
250. Yuan, K., Zhang, X., Li, L. & Tang, D. Effects of tensile strain and finite size on thermal conductivity in monolayer WSe_2. *Phys. Chem. Chem. Phys.* **21**, 468–477 (2019).
251. Raeisi, M., Ahmadi, S. & Rajabpour, A. Modulated thermal conductivity of 2D hexagonal boron arsenide: a strain engineering study. *Nanoscale* **11**, 21799–21810 (2019).
252. Duffy, T. S. Synchrotron facilities and the study of the Earth's deep interior. *Rep. Prog. Phys.* **68**, 1811–1859 (2005).
253. Shen, G. & Mao, H.-K. High-pressure studies with x-rays using diamond anvil cells. *Rep. Prog. Phys.* **80**, 016101 (2016).
254. Lin, J.-F., Alp, E. E. & Goncharov, A. F. in *Treatise on Geochemistry* 2nd edn Vol. 15 (eds Holland, H. D. & Turekian, K. K.) 195–211 (Elsevier, 2014).
255. Lay, T., Hernlund, J. & Buffett, B. A. Core–mantle boundary heat flow. *Nat. Geosci.* **1**, 25–32 (2008).
256. Nimmo, F. in *Treatise on Geophysics* 2nd edn (ed. Schubert, G.) 27–55 (Elsevier, 2015).
257. Moroe, S. et al. Measurements of hydrogen thermal conductivity at high pressure and high temperature. *Int. J. Thermophys.* **32**, 1887–1917 (2011).
258. Johns, A. I., Rashid, S., Rowan, L., Watson, J. T. R. & Clifford, A. A. The thermal conductivity of pure nitrogen and of mixtures of nitrogen and carbon dioxide at elevated temperatures and pressures. *Int. J. Thermophys.* **9**, 3–19 (1988).
259. Michels, A., Sengers, J. V. & Van De Klundert, L. J. M. The thermal conductivity of argon at elevated densities. *Physica* **29**, 149–160 (1963).
260. Parrish, K. D., Jain, A., Larkin, J. M., Saidi, W. A. & McGaughey, A. J. H. Origins of thermal conductivity changes in strained crystals. *Phys. Rev. B* **90**, 235201 (2014).
261. Ross, R. G., Andersson, P. & Bäckström, G. Thermal conductivity of allotropic modifications of ice. *Nature* **259**, 553–554 (1976).
262. Elalfy, L., Music, D. & Hu, M. First principles investigation of anomalous pressure-dependent thermal conductivity of chalcopyrites. *Materials* **12**, 3491 (2019).
263. Harish, S. et al. Thermal conductivity reduction of crystalline silicon by high-pressure torsion. *Nanoscale Res. Lett.* **9**, 326 (2014).
264. Kuryliuk, V., Nepochatyi, O., Chantrenne, P., Lacroix, D. & Isaiev, M. Thermal conductivity of strained silicon: molecular dynamics insight and kinetic theory approach. *J. Appl. Phys.* **126**, 055109 (2019).
265. Xie, H. et al. Large tunability of lattice thermal conductivity of monolayer silicene via mechanical strain. *Phys. Rev. B* **93**, 075404 (2016).
266. Bridgman, P. W. The thermal conductivity and compressibility of several rocks under high pressures. *Am. J. Sci.* **7**, 81–102 (1924).

Acknowledgements
The authors thank H.-K. Mao for the encouragement in the technique development and research. The Center for High Pressure Science & Technology Advanced Research (HPSTAR, Shanghai), Harbin Institute of Technology (HIT, Shenzhen), Academia Sinica (Taipei) and the Carnegie Institution for Science (Washington DC) are gratefully acknowledged for support. This work is funded through the Shenzhen Science and Technology Program (grant no. KQTD20200820113043508) and the Basic Research Program of Shenzhen (grant no. JCYJ20200109112810241) at HIT and the National Key R&D Program of China (grant no. 2018YFA0305900) at HPSTAR. W.-P.H. acknowledges support from Academia Sinica and the Ministry of Science and Technology of Taiwan under contracts AS-CDA-106-M02 and 107-2628-M-001-004-MY3, as well as the fellowship from the Foundation for the Advancement of Outstanding Scholarship of Taiwan. The work at Carnegie is supported by the US National Science Foundation (grant nos. EAR-1763287 and EAR-2049127).

Author contributions
X.-J.C. designed the project and developed the outline of this work. Y.Z., Z.-Y.D. and X.-J.C. compiled all the data in the tables. Z.-Y.D. and Y.Z. drew the figures. All authors contributed to the discussion of content and the preparation of the manuscript in collaboration.

Competing interests
The authors declare no competing interests.

Peer review information
Nature Reviews Physics thanks the anonymous referees for their contribution to the peer review of this work.

Publisher's note
Springer Nature remains neutral with regard to jurisdictional claims in published maps and institutional affiliations.

Supplementary information
The online version contains supplementary material available at https://doi.org/10.1038/s42254-022-00423-9.